DEPARTMENT OF PHYSICS
UNIVERSITY OF JYVÄSKYLÄ
RESEARCH REPORT No. 16/2009

NUMERICAL STUDIES ON MEMBRANE CRUMPLING

BY
TUOMAS TALLINEN

Academic Dissertation
for the Degree of
Doctor of Philosophy

To be presented, by permission of the
Faculty of Mathematics and Natural Sciences
of the University of Jyväskylä,
for public examination in Auditorium FYS-1 of the
University of Jyväskylä on December 10th, 2009
at 12 o'clock noon

Jyväskylä, Finland
November 2009

Preface

The work reported in this Thesis was done during the years 2006-2009 in the Department of Physics at the University of Jyväskylä.

I have had the fortune to be supervised by Professor Jussi Timonen, whose motivating and encouraging guidance throughout the work made this thesis realise. I'm grateful to Dr. Jan Åström for guiding me when starting this work, for his contribution to the research and for many inspiring discussions. I got important advice also from Dr. Pekka Kekäläinen.

I thank all the colleagues in the SoftStat group for advice and good time during the years: Keijo Mattila, Jari Hyväluoma, Jarno Alaraudanjoki, Vantte Kilappa, Juho Ojajärvi and the people at FL348 and FL220.

Financial support from the University of Jyväskylä, Jyväskylä Innovation and the Finnish Cultural Foundation are greatly acknowledged. For computational resources I thank the Finnish IT Center for Science, CSC.

Jyväskylä, November 2009

Tuomas Tallinen

Abstract

In this Thesis crumpling of thin sheets is explored when they are confined into a small volume by external forcing. To this end a simulation model based on a discrete element method is constructed. The Thesis begins with an introductory part reviewing the related elasticity theory and previous results on the properties of relevant geometric structures, ridges and cones, which appear in crumpled sheets. Results are reported for elastic and plastic thin sheets, and elastic sheets with self adhesion.

Crumpling of elastic sheets was found to exhibit deterministic features and efficient packing of the sheet. Real materials at macroscopic scale are, however, elasto-plastic. By including plasticity we found that the crumpling process became random in agreement with everyday experience, and found that in contrast with intuitive expectations it is harder to crumple a plastic sheet.

At microscopic scales van der Waals interactions and thermal fluctuations are essential for conformations of thin sheets. These effects are included in the simulations realized by Langevin dynamics. An intriguing question of whether adhesive interactions and thermal fluctuations would induce crumpling, even in the absence of external forcing, is discussed. Stability of microscopic membranes is explained in terms of membrane stiffness, adhesion strength and temperature.

Author's address Tuomas Tallinen
Department of Physics
University of Jyväskylä
Finland

Supervisors Professor Jussi Timonen
Department of Physics
University of Jyväskylä
Finland

Doctor Jan Åström
CSC - IT Center for Science
Finland

Reviewers Professor Gerhard Gompper
Institute of Solid State Research
University of Cologne
Germany

Professor Mikko Karttunen
Department of Applied Mathematics
University of Western Ontario
Canada

Opponent Professor Alex Hansen
Department of Physics
Norwegian University of Science and Technology
Norway

List of Publications

I T. Tallinen, J. A. Åström and J. Timonen, *Deterministic folding in stiff elastic membranes*, Physical Review Letters **101**, 106101 (2008)

II T. Tallinen, J. A. Åström and J. Timonen, *The effect of plasticity in crumpling of thin sheets*, Nature Materials **8**, 25-29 (2009)

III T. Tallinen, J. A. Åström and J. Timonen, *Discrete element simulations of crumpling of thin sheets*, Computer Physics Communications **180**, 512-516 (2009)

IV T. Tallinen, J. A. Åström, P. Kekäläinen and J. Timonen, *Stability and crumpling of adhesive membanes with nonzero bending rigidity*, submitted

The author of this thesis wrote the drafts of the papers [II], [III] and [IV] and parts of the paper [I]. The author participated in planning the research, did the numerical work in all papers and contributed to the analytical calculations in the paper [IV]. Simulation programs were developed by the author based on the original numerical code by J. Å.

Contents

1 Introduction

Thin sheets, or membranes, are objects which are much larger in two of the spatial dimensions than in the third one. Such objects are common in the nature at almost all length scales. The thinnest sheets known are only one atom thick, as for example a sheet of carbon atoms, called graphene, while among the thickest is the crust of the earth. The common examples in between include cell membranes, aluminium foil, paper, polymeric packing materials and metallic sheets used in e.g. car chassis. The present work considers crumpling of such a thin sheet, when it is confined into a small volume by external forcing. Crumpling of thin sheets has previously been demonstrated to exhibit for instance fascinating stress condensation phenomena [68]. Stress condensation can be observed as a formation of a network of ridges and sharp vertices when e.g. a sheet of paper is crumpled.

Behaviour of membranes became an active field of research in the late 1980s. The most of the early studies was devoted to thermally fluctuating membranes and the related statistical mechanics, for a variety of model membranes [18, 19, 21, 22, 24, 25, 26]. These membranes were classified as fixed connectivity or fluid membranes depending on their internal connectivity, and phantom or self-avoiding if they were allowed to intersect themselves or not. Furthermore, fixed connectivity membranes were flexible (no bending rigidity) or rigid. There are no realizations of phantom membranes or of purely flexible ones, so these membrane classes have served as theoretical simplifications. Examples of self-avoiding, rigid, fixed connectivity membranes include graphene and macroscopic sheets, and those of fluid membranes include lipid bilayer membranes of vesicles and cells. This Thesis mostly considers self-avoiding, rigid, fixed connectivity membranes. The word membrane is used as a synonym for a thin sheet in this Thesis.

An important question in the statistical mechanics of membranes is the existence of entropy induced crumpling. Analysis by the renormalization group method have revealed a crumpling transition of phantom membranes [12]. Self-avoidance makes the analytical treatment very difficult, but simulation results indicate absence of the crumpling transition in self-avoiding fixed connectivity membranes [12, 48, 49]. They seem to preserve long range orientation order and an infinite persistence length at any temperature. It seems however that self-avoidance does not prevent crumpling of fluid membranes [31]. The reason for why the membranes of our cells do not appear crumpled is that the persistence length is much higher than their size. An interesting question still remains whether attractive interactions will change the conclusion

concerning the existence of crumpling in microscopic world.

Research on the statistical mechanics of fluctuating membranes seems to have slowed down during the last decade. Since the 1990s there has been, however, significant interest in the mechanics and geometry of forced crumpling of thin sheets [37, 41, 44, 50, 53, 63]. Much of the theoretical progress in this direction has been related to explaining the properties of isolated singular features like ridges [37, 40] and vertices [44, 54, 59] that appear in crumpled sheets. Due to the complexity of the full process, one has to rely on simulations or experiments when it comes to questions such as how the network of ridges and vertices is formed and behaves under crumpling, and how external and material parameters affect this process. Experiments on forced crumpling are easy to carry out as possible sheet materials (paper, aluminium foil etc.) are conveniently available everywhere. There are useful data available from experiments [23, 53, 60, 70, 71, 72, 73, 78], but some experimental parameters such as plasticity, friction and external forcing are rather difficult to control accurately. It is also difficult to measure in detail, e.g., the energy and exact geometry of the sheet during crumpling.

Simulations offer a possibility for highly controlled crumpling 'experiments', and by including thermal fluctuation and attractive van der Waals like interaction they can be extended to model behaviour of membranes at microscopic scales. Previous simulations related to crumpling include Monte Carlo and molecular dynamics simulations of thermally fluctuating membranes [22, 28, 25, 48], simulations of single ridges and vertices by energy minimization algorithms [24, 59, 50, 40], and molecular dynamics or discrete element simulations of forced crumpling at effectively zero temperature [41, 43, 58, 63, 75].

A discrete element method is used in the present work to simulate crumpling of thin sheets. With the discrete element method very complex dynamics of a large set of deformable elements can be simulated. The number of elements is so high and their interactions are so complicated that explicit methods are used to solve their equations of motion. In that sense the method resembles molecular dynamics. A feasible lattice size of a sheet is currently around million points, which makes it possible to simulate sheets of realistic size.

In Chapter 2 we review some relevant aspects of the elasticity theory for thin sheets, and we also review the mechanics and geometry behind a single ridge, as it is the most fundamental building block in crumpling. The discrete element models that are used in the crumpling simulations are described in Chapter 3. Two approaches are described for modeling the intrinsic deformability of the sheet, as well as for modeling self-avoidance. Implementation issues and parallelization are also discussed. The main results of this Thesis are reviewed in Chapters 4 (papers I, II and III) and 5 (paper IV).

In Chapter 4 we study crumpling of ideal fully elastic and frictionless sheets and com-

pare that process to crumpling of 'realistic like' elasto-plastic sheets. We are interested in the statistical properties of crumpled geometry and how the previous theories for a single ridge can be used to describe full-scale crumpling. Previous simulations and theory have considered only elastic sheets, but real materials are elasto-plastic, meaning that large strains are irreversible. Exploring that effect is important for bridging theory and simulations with experiment.

At microscopic scales attractive interactions are present, and they have been included in the studies presented in Chapter 5. Thermal fluctuations are also included by the Langevin method. These simulations were motivated by previous studies of adhesive membranes, which have only considered flexible membranes. Crumpling under external force of fluctuating membranes has also been an unexplored area. An interesting application of the studies of Chapter 5 is the behaviour of graphene under external loading.

In chapter 6 we draw some conclusions about our main results and discuss possible future directions. Thesis ends with an application to vertical compression of thin-walled boxes in appendix A.

2 Deformations of thin sheets

2.1 Strain, curvature and energy of a deformed sheet

We consider a sheet of isotropic elastic material with a flat metric in an undeformed configuration. The sheet is assumed to be thin enough so it can be regarded as a two-dimensional surface. In such a case sheet deformations can be separated in to in-plane stretching and bending [3]. The formulation presented here applies to a case where the sheet is allowed to undergo large deflections but to have only small strains. This is compatible with crumpling, as large strains are expected to carry only a small fraction of the total deformation energy and concentrate into a small area fraction of the sheet at and near the tips of the vertices [68].

In the following we denote by $\mathbf{x} = (x_1, x_2, x_3)$ material coordinates, where x_1 and x_2 are planar coordinates and x_3 is a coordinate in the thickness direction of the sheet. Position in space of a material point $\mathbf{x}$ is given by $\mathbf{r} = (u_1, u_2, u_3)$. The metric tensor $\mathbf{g}$ together with its relation to the strain tensor $\boldsymbol{\gamma}$ is given by

$$g_{ij} = \frac{\partial \mathbf{r}}{\partial x_i} \cdot \frac{\partial \mathbf{r}}{\partial x_j} = \delta_{ij} + 2\gamma_{ij}. \tag{2.1}$$

According to Hooke's law the deformation energy is proportional to the square of the strain. Since energy is a scalar quantity it can only depend on the quadratic invariants of the strain tensor. These can be taken to be $(\operatorname{Tr} \boldsymbol{\gamma})^2$ and $\operatorname{Tr} \boldsymbol{\gamma}^2$ leading to the expression

$$F = \frac{1}{2}\lambda (\operatorname{Tr} \boldsymbol{\gamma})^2 + \mu \operatorname{Tr} \boldsymbol{\gamma}^2 \tag{2.2}$$

for the deformation energy density. Here λ and μ are the Lamé coefficients of the material. It is more convenient to express the energy in terms of Young's modulus Y and Poisson's ratio ν. Their relation to the Lamé coefficients is given by [3]

$$\lambda = \frac{Y\nu}{(1-2\nu)(1+\nu)}, \tag{2.3}$$

$$\mu = \frac{Y}{2(1+\nu)}. \tag{2.4}$$

The Young's modulus of a material is defined as the ratio of the uniaxial stress to the uniaxial strain. When a material is stretched in one direction it typically contracts in the other directions. Poisson's ratio measures the ratio of this contraction to the amount of stretching. The free energy density expressed in terms of Y and ν is

$$F = \frac{Y}{2(1+\nu)}\left(\operatorname{Tr}\boldsymbol{\gamma}^2 + \frac{\nu}{1-2\nu}(\operatorname{Tr}\boldsymbol{\gamma})^2\right). \tag{2.5}$$

For determining the energy of a deformed sheet we first consider the contribution of in-plane strain, i.e. stretching deformations. The components of the in-plane strain tensor $\boldsymbol{\epsilon}$ are

$$\begin{aligned}
\epsilon_{11} &= \frac{1}{2}\left[\left(\frac{\partial \mathbf{r}}{\partial x_1}\right)^2 - 1\right], \\
\epsilon_{22} &= \frac{1}{2}\left[\left(\frac{\partial \mathbf{r}}{\partial x_2}\right)^2 - 1\right], \\
\epsilon_{12} &= \epsilon_{21} = \frac{1}{2}\left(\frac{\partial \mathbf{r}}{\partial x_1}\cdot\frac{\partial \mathbf{r}}{\partial x_2}\right).
\end{aligned} \tag{2.6}$$

The stretching energy S is found by integrating equation (2.5) over the area A and thickness h of the sheet, which gives

$$S = \frac{Yh}{2(1+\nu)}\int_A \left[\operatorname{Tr}\boldsymbol{\epsilon}^2 + \frac{\nu}{1-2\nu}(\operatorname{Tr}\boldsymbol{\epsilon})^2\right] dA. \tag{2.7}$$

In order to determine the contribution of bending to the total deformation energy we introduce the curvature tensor

$$C_{ij} = \mathbf{n}\cdot\frac{\partial^2 \mathbf{r}}{\partial x_i \partial x_j}, \tag{2.8}$$

where $i, j = 1, 2$ and $\mathbf{n}$ is the normal of the midplane surface $x_3 = 0$. Curvature of the sheet results in a strain given by

$$\begin{aligned}
\gamma_{11} &= -x_3 C_{11}, \\
\gamma_{22} &= -x_3 C_{22}, \\
\gamma_{12} &= -x_3 C_{12}, \\
\gamma_{33} &= \frac{\nu}{1-\nu} x_3 (C_{11} + C_{22}), \\
\gamma_{23} &= \gamma_{13} = 0.
\end{aligned} \tag{2.9}$$

The free energy per unit volume associated with bending is found from equation (2.5). Integrating F over the thickness and area of the sheet yields

$$B = \kappa \int_A \left\{\frac{1}{2}(\operatorname{Tr}\mathbf{C})^2 + (1-\nu)\left[\operatorname{Tr}\mathbf{C}^2 - (\operatorname{Tr}\mathbf{C})^2\right]\right\} dA, \tag{2.10}$$

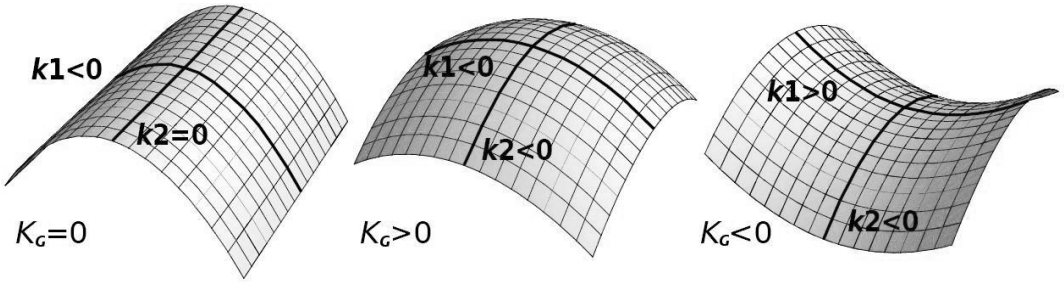

Figure 2.1: The surface on the left has curvature only in one direction and its Gaussian curvature is $K_G = k_1 k_2 = 0$. The surface in the middle has both principal curvatures in the same direction resulting in a positive Gaussian curvature. The surface on the right has principal curvatures of opposite sign and the resulting Gaussian curvature is negative.

where $\kappa = \frac{Yh^3}{12(1-\nu^2)}$ is the bending modulus.

The total deformation energy of the sheet is $S + B$. The ratio of stretching to bending energy for a given configuration of the sheet is of the order of $Eh/\kappa \sim h^{-2}$, which means that for thin membranes stretching is expensive in comparison with bending. Configurations of a thin sheet are thus unavoidably close to isometric transformations, meaning that distances along the sheet are approximately preserved under deformation.

Eigenvalues of the curvature tensor, k_1 and k_2, are the principal curvatures related to the minimum and maximum curvature at the point considered. The two invariants of the curvature tensor, $H = (k_1 + k_2)/2$ and $K_G = k_1 k_2$, are called the mean and Gaussian curvature, respectively. The principal curvatures and Gaussian curvature are illustrated in figure 2.1. An important aspect of Gaussian curvature is that its change affects the internal metric of the surface. For a sheet with flat undeformed metric this means that Gaussian curvature necessary produces strain. This connection results from Gauss's Theorema Egregium [68],

$$K_G = 2\partial_1\partial_2\epsilon_{12} - \partial_1\partial_1\epsilon_{22} - \partial_2\partial_2\epsilon_{11} + O(\boldsymbol{\epsilon}^2). \tag{2.11}$$

2.2 Determination of strain and curvature

The two dimensional in-plane strain and curvature introduced above are useful in describing the deformations of a thin sheet. In this section we present methods to estimate them on a regular triangular lattice.

We express the elements of the strain tensor $\boldsymbol{\epsilon}$ in terms of the basis vectors $\mathbf{b}_1$ and $\mathbf{b}_2$

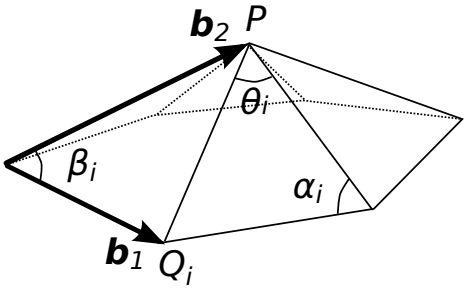

Figure 2.2: A small part of a deformed triangular lattice.

of the basic cell of the lattice (lattice constant a) [12]. The basis vectors are indicated in figure 2.2. The undeformed angle between these basis vectors is $\pi/3$. We form the vector $\mathbf{g} = (2\mathbf{b}_2 - \mathbf{b}_1)/\sqrt{3}$ that is perpendicular to $\mathbf{b}_1$. The elements of the strain tensor are now given by

$$\begin{aligned} \epsilon_{11} &= (\mathbf{b}_1^2/a^2 - 1)/2, \\ \epsilon_{12} &= \epsilon_{21} = \mathbf{b}_1 \cdot \mathbf{g}/(2a)^2, \\ \epsilon_{22} &= (\mathbf{g}^2/a^2 - 1)/2. \end{aligned} \tag{2.12}$$

An estimate for the mean curvature is found by noticing that it is given by the divergence of the surface normal: $H = \nabla \cdot \mathbf{n}$. By a fairly simple algebra one can show that [45], for a vertex P,

$$-H\mathbf{n} = \frac{1}{4A} \sum_i (\cot \alpha_i + \cot \beta_i)(\mathbf{q}_i - \mathbf{p}), \tag{2.13}$$

where $\{Q_i\}$ are the neighbour vertices of P, α_i and β_i are the two angles opposite to the edge Q_iP, $\mathbf{q}_i$ and $\mathbf{p}$ are the positions of Q_i and P, respectively, and $A = \sum_i A_i$ is the area of the triangles surrounding P, see figure 2.2.

Estimation of the Gaussian curvature K_G relies on its close connection to the angle deficit $\Delta\Theta$, which is defined for a vertex of a polygonal surface as $\Delta\Theta = 2\pi - \sum_i \Theta_i$. Here $\{\Theta_i\}$ are the angles between the adjacent edges connected to the vertex, see figure 2.2. Since the integral of the Gaussian curvature over some area is the total angle deficit in that area, and the area related to the vertex is $\sum_i A_i/3$, we find approximately that

$$K_G = 3\Delta\Theta / \sum_i A_i. \tag{2.14}$$

2.3 The elastic loop

In this section we consider a strip of thin sheet bent half a round such that the ends become parallel and touch each other. Solving for properties of such a deformation finds application in Chapter 5 dealing with adhesive sheets. As a result of minimization of elastic bending energy, the bent loop assumes a smooth shape as illustrated in figure 2.3. For a strip of length l and width L the elastic energy of the loop can be expressed in the form

$$E_{el} = \frac{1}{2}\kappa L \int_0^l C(t)^2 dt, \tag{2.15}$$

where C is the curvature of the loop and integration is along the cross section. Curvature $C(t)$ is related to the directional angle $\Theta(t)$ between the loop and its middle plane such that $C = \frac{d\Theta}{dt} = \Theta'$. The loop is obviously symmetric with respect to its middle plane so we may focus only on the first half of the loop: $0 < t < l/2$. Boundary conditions for the angle are $\Theta(0) = 0$ and $\Theta(l/2) = -\pi/2$, and symmetry requires that

$$\int_0^{l/2} \sin\Theta dt = 0. \tag{2.16}$$

In order to find the curvature that minimizes the elastic energy [20], we use the multiplier method of variational calculus [2], and consider the functional

$$H = \int_0^{l/2} F(\Theta, \Theta')dt = \int_0^{l/2} \left(\Theta'^2 + \lambda \sin\Theta\right) dt. \tag{2.17}$$

The Euler equation for $F(\Theta, \Theta')$ is then given as [2]

$$F - \Theta' \frac{dF}{d\Theta'} = const = -C_0^2 \tag{2.18}$$

so that

$$\Theta'^2 - \lambda \sin\Theta = C_0^2. \tag{2.19}$$

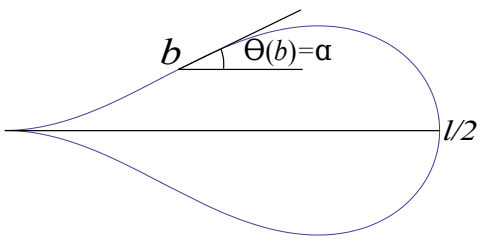

Figure 2.3: An elastic loop of length l. The directional angle Θ takes a universal value $\alpha \approx 28°$ at point b, at which the curvature changes sign.

By recalling that $C = \Theta'$, and by writing the constant λ as $\lambda = -C_0^2/\sin\alpha$, we find that the curvature of the cross section of the loop is

$$\begin{aligned} C &= C_0\sqrt{1-\frac{\sin\Theta}{\sin\alpha}}; \quad t < b, \\ C &= -C_0\sqrt{1-\frac{\sin\Theta}{\sin\alpha}}; \quad t > b. \end{aligned} \tag{2.20}$$

Here the constant $\alpha \approx 27.54°$ is the angle at the point $b \approx 0.163l$ at which the curvature changes sign, and $C_0 \approx 6.05/l$. By equation (2.15) we find the loop's elastic energy,

$$E_{el} = a\kappa L/l, \quad a \approx 18.33. \tag{2.21}$$

The constants here were found by numerical integration of equation (2.20). The energy can also be expressed in terms of elliptic integrals as

$$\begin{aligned} E &= \kappa L\left(\int_0^b C(t)^2\,dt + \int_b^{l/2} C(t)^2\,dt\right) \\ &= \kappa L C_0\left(\int_0^\alpha \sqrt{1-\frac{\sin\Theta}{\sin\alpha}}\,d\theta - \int_\alpha^{-\pi/2}\sqrt{1-\frac{\sin\theta}{\sin\alpha}}\,d\theta\right) \\ &= \frac{\sqrt{2}\,\kappa L C_0}{\sqrt{\sin\alpha}}\left\{4\,E(k) - 2\,E(\gamma,k) - (1-\sin\alpha)\left[2\,K(k) - F(\gamma,k)\right]\right\}, \end{aligned} \tag{2.22}$$

where

$$k = \sqrt{\frac{\sin\alpha+1}{2}}, \qquad \gamma = \arcsin\sqrt{\frac{1}{\sin\alpha+1}}, \tag{2.23}$$

and E, F and K are the elliptic integrals [4]

$$\begin{aligned} E(\phi,k) &= \int_0^\phi \sqrt{1-k^2\sin^2\theta}\,d\theta, \\ F(\phi,k) &= \int_0^\phi \frac{d\theta}{\sqrt{1-k^2\sin^2\theta}}, \\ E(k) &= E(\pi/2,k), \quad K(k) = F(\pi/2,k). \end{aligned} \tag{2.24}$$

The constant C_0 in terms of elliptic integrals can be determined from the equation

$$\begin{aligned} \frac{l}{2} &= \int_0^b dt + \int_b^{l/2} dt \\ &= \frac{\sqrt{\sin\alpha}}{C_0}\left(\int_0^\alpha \frac{d\theta}{\sqrt{\sin\alpha-\sin\theta}} - \int_\alpha^{-\pi/2}\frac{d\theta}{\sqrt{\sin\alpha-\sin\theta}}\right) \\ &= \frac{\sqrt{2\sin\alpha}}{C_0}\left[2\,K(k) - F(\gamma,k)\right], \end{aligned} \tag{2.25}$$

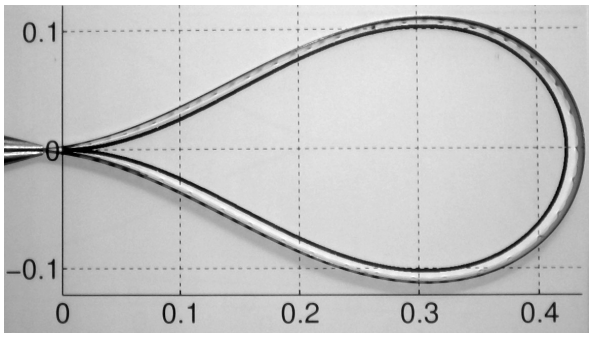

Figure 2.4: The theoretical shape of an elastic loop of unit length (inner line) is compared with that of a bent metal blade (outer line).

but, however, the angle α remains to be determined numerically. An experimental confirmation for the shape of the loop is shown in figure 2.4.

2.4 The ridge and cone singularities

In the thin sheet limit, $h \to 0$, stretching becomes energetically prohibited, and the membrane configurations are strictly isometric. However, it is not possible to confine an unstretchable two-dimensional surface into a small three-dimensional volume by only smooth deformations [46]. Such confinement necessarily requires folding along sharp lines and vertices. For non-zero thickness these singular lines and vertices would have infinite bending energy. What happens is that these singularities smoothen resulting in a balance between stretching and bending [6, 33, 37, 47]. In this section properties of the resulting geometric structures, line-like ridges and point-like vertices, are briefly reviewed.

An elastic ridge is very important in crumpling. We present here geometric reasoning to derive its properties. The derivation follows that of Lobkovsky's [37]. We consider a thin sheet of width X bent sharply as in figure 2.5. The transverse curvature between the rigidly fastened sides relaxes assuming a value C_r at the mid-ridge, such that the ridge line must deflect away from its original position by an amount ζ_r of the order of $1/C_r$. This deflection results in stretching $\gamma \simeq (\zeta_r/C_r)^2$ at the ridge line. The bulk of the deformation is concentrated on a strip of width $w \simeq 1/C_r$ so that the stretching energy of the strip is

$$S = Yh \int \gamma^2 dA \sim Yh\gamma^2 Xw \sim YhX^{-3}C_r^{-5}. \tag{2.26}$$

The energy to bend the strip is given by

$$B \sim \kappa C_r^2 Xw \sim Yh^3 XC_r. \tag{2.27}$$

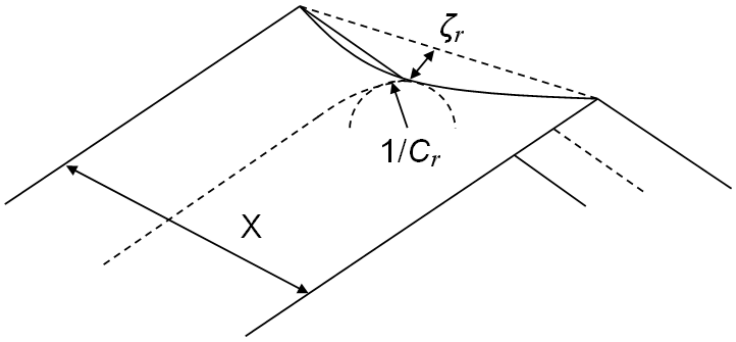

Figure 2.5: Illustration of a ridge formed by bending a strip of thin sheet. The strip width X, sag ζ_r and radius of curvature $1/C_r$ in the middle of the ridge are indicated.

Figure 2.6: Loosely crumpled aluminium foil displaying a network of ridges meeting at sharp vertices.

Minimizing the sum of these two energy components requires that $C_r \simeq (1/X)(X/h)^{1/3}$, and the energy E_r of an optimal configuration is of the order of $\kappa(X/h)^{1/3}$.

Vanishing of the derivative of E_r with respect to C_r leads to another important conclusion [68]:

$$\frac{dE_r}{dC_r} = \frac{dS}{dC_r} + \frac{dB}{dC_r} = \frac{-5S}{C_r} + \frac{B}{C_r} = 0, \tag{2.28}$$

indicating that $B = 5S$ for ridges.

Lobkovsky also performed an asymptotic analysis of the Föppl-von Kármán equations [3] for the ridge setup, and ended up with agreement with the above reasoning [40].

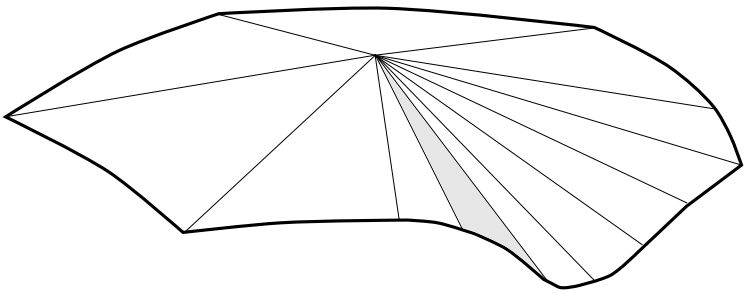

Figure 2.7: Developable cone in a loosely confined sheet.

A more detailed analysis of the energy of a ridge leads to

$$E_r \approx F_r \kappa \left(\frac{X}{h}\right)^{1/3} \phi^{7/3}, \tag{2.29}$$

in which also the bending angle ϕ is included [40, 68]. The constant $F_r \approx 1$ can be determined numerically. Ridges are clearly observed in a confined thin sheet, as e.g. in that of figure 2.6.

In addition to a ridge, there is another perhaps even more fundamental singularity that appears in crumpled sheets: a developable cone or d-cone. These cone-like structures with a sharp vertex appear as endpoints of a ridge or alone in a gently confined sheet, as in figure 2.7. The energy of an isolated d-cone is given by [44, 47]

$$E_d \approx F_d \kappa \ln\left(\frac{R}{R_C}\right) \phi^2, \tag{2.30}$$

where R is the size of the cone, ϕ the complement of the tip angle of the cone, and

$$R_C \approx (\kappa/Yh)^{1/6} R^{2/3} \phi^{-1/3} \tag{2.31}$$

is the radius of the core of the d-cone, i.e., the crescent-shaped region on which stretching is concentrated [59]. The constant F_d above is $F_d \approx 100$ [47].

By qualitatively comparing the energies of a ridge and a d-cone it is evident that, in a very thin sheet with sharp ridges, the ridge energy dominates. That is the typical case in crumpling. However, for a weakly confined sheet with just a few gentle singularities the d-cone energy can be relevant.

3 Modeling a thin sheet

3.1 Deformable beam elements

A model for a thin sheet of elastic or elasto-plastic material is constructed as a triangular lattice. Each lattice point has mass m and moment of inertia I, and they are connected by identical beam elements. The width and length of the beam are the same as the lattice constant a, and its thickness is the same as the sheet thickness h. The motion of a beam is governed by

$$M\ddot{\mathbf{u}} = C\dot{\mathbf{u}} + K\mathbf{u}, \tag{3.1}$$

where M, C and K are the 12x12 mass, damping and stiffness matrices, respectively. Vector $\mathbf{u}$ contains the deformations of the beam (three translational and three rotational degrees of freedom at both ends of the beam):

$$\mathbf{u} = [u_{x1} \quad u_{y1} \quad u_{z1} \quad \Theta_{x1} \quad \Theta_{y1} \quad \Theta_{z1} \quad u_{x2} \quad u_{y2} \quad u_{z2} \quad \Theta_{x2} \quad \Theta_{y2} \quad \Theta_{z2}]^{\mathrm{T}}. \tag{3.2}$$

We use a standard stiffness matrix for a 3-dimensional beam element with shear effects accounted for, see table 2.1. For detailed derivation of the matrix see reference [7]. The familiar geometric moments I_x, I_y and I_z of the cross-sections that appear in the stiffness matrix are given by

$$I_x = ah^3(0.33 - 0.19h/a), \quad I_y = ah^3/12, \quad I_z = a^3h/12. \tag{3.3}$$

The mass matrix is diagonal, and the damping matrix is given by the mass matrix and the diagonal part of the stiffness matrix such that $C \sim \sqrt{MK_{diag}}$. The magnitude of damping is chosen so that the motion of any single beam is under-damped. The stiffness (Young's modulus) of the beam is Y and its Poisson ratio is $\nu = 1/3$ resulting in the bending modulus $\kappa \approx 0.1Yh$ for the sheet.

Crumpling involves large displacements and rotations of beams although their actual deformations are not necessarily large. The rigid body motion of a beam is separated from its deformation $\mathbf{u}$ by attaching to it a coordinate frame which retains only the deformation part of the total motion. This kind of formulation for handling large displacements has been used in a finite element method (FEM) and in a computer animation [15].

$$\begin{bmatrix}
\frac{YA}{L} & 0 & 0 & 0 & 0 & 0 & -\frac{YA}{L} & 0 & 0 & 0 & 0 & 0 \\
0 & \frac{12YI_z}{L^3(1+\phi_y)} & 0 & 0 & 0 & \frac{6YI_z}{L^2(1+\phi_y)} & 0 & -\frac{12YI_z}{L^3(1+\phi_y)} & 0 & 0 & 0 & \frac{6YI_z}{L^2(1+\phi_y)} \\
0 & 0 & \frac{12YI_y}{L^3(1+\phi_z)} & 0 & -\frac{6YI_y}{L^2(1+\phi_z)} & 0 & 0 & 0 & -\frac{12YI_y}{L^3(1+\phi_z)} & 0 & -\frac{6YI_y}{L^2(1+\phi_z)} & 0 \\
0 & 0 & 0 & \frac{GI_x}{L} & 0 & 0 & 0 & 0 & 0 & -\frac{GI_x}{L} & 0 & 0 \\
0 & 0 & -\frac{6YI_y}{L^2(1+\phi_z)} & 0 & \frac{(4+\phi_z)YI_y}{L(1+\phi_z)} & 0 & 0 & 0 & \frac{6YI_y}{L^2(1+\phi_z)} & 0 & \frac{(2-\phi_z)YI_y}{L(1+\phi_z)} & 0 \\
0 & \frac{6YI_z}{L^2(1+\phi_y)} & 0 & 0 & 0 & \frac{(4+\phi_y)YI_z}{L(1+\phi_y)} & 0 & -\frac{6YI_z}{L^2(1+\phi_y)} & 0 & 0 & 0 & \frac{(2-\phi_y)YI_z}{L(1+\phi_y)} \\
-\frac{YA}{L} & 0 & 0 & 0 & 0 & 0 & \frac{YA}{L} & 0 & 0 & 0 & 0 & 0 \\
0 & -\frac{12YI_z}{L^3(1+\phi_y)} & 0 & 0 & 0 & -\frac{6YI_z}{L^2(1+\phi_y)} & 0 & \frac{12YI_z}{L^3(1+\phi_y)} & 0 & 0 & 0 & -\frac{6YI_z}{L^2(1+\phi_y)} \\
0 & 0 & -\frac{12YI_y}{L^3(1+\phi_z)} & 0 & \frac{6YI_y}{L^2(1+\phi_z)} & 0 & 0 & 0 & \frac{12YI_y}{L^3(1+\phi_z)} & 0 & \frac{6YI_y}{L^2(1+\phi_z)} & 0 \\
0 & 0 & 0 & -\frac{GI_x}{L} & 0 & 0 & 0 & 0 & 0 & \frac{GI_x}{L} & 0 & 0 \\
0 & 0 & -\frac{6YI_y}{L^2(1+\phi_z)} & 0 & \frac{(2-\phi_z)YI_y}{L(1+\phi_z)} & 0 & 0 & 0 & \frac{6YI_y}{L^2(1+\phi_z)} & 0 & \frac{(4+\phi_z)YI_y}{L(1+\phi_z)} & 0 \\
0 & \frac{6YI_z}{L^2(1+\phi_y)} & 0 & 0 & 0 & \frac{(2-\phi_y)YI_z}{L(1+\phi_y)} & 0 & -\frac{6YI_z}{L^2(1+\phi_y)} & 0 & 0 & 0 & \frac{(4+\phi_y)YI_z}{L(1+\phi_y)}
\end{bmatrix}$$

$$\phi_y = \frac{12YI_z}{AGL^2} \qquad \phi_z = \frac{12YI_y}{AGL^2}$$

Table 2.1 Stiffness matrix for a beam element. Here A is the area of the cross-section, L the length of the beam and $G = \frac{Y}{2(1+\nu)}$ the shear modulus.

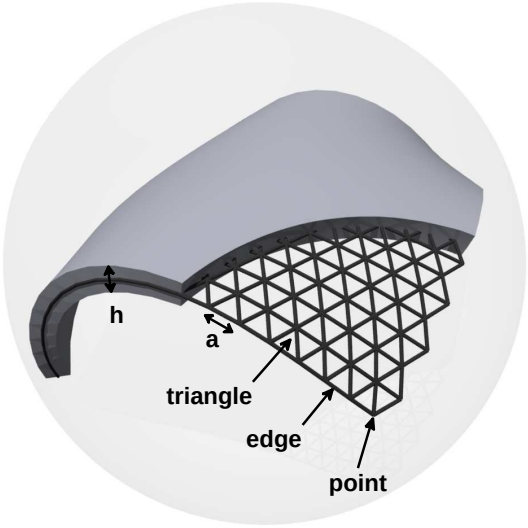

Figure 3.1: Illustration of our discrete element model of a thin sheet. A part of the underlying triangular lattice is shown, and the sheet thickness h, lattice constant a and geometrical primitives (a point, an edge and a triangle) are indicated.

To account for elasto-plasticity, elastic-perfectly plastic stress-strain relations are assumed for stretching, torsion and bending of each beam. The yield points of these deformation modes are proportional to the yield stress σ_s of the material. For a longitudal force, the torsion moment and bending moments they are

$$F_s = ha\sigma_s, \quad M_{xs} = 0.58\sigma_s I_x/h, \quad M_{ys} = 2\sigma_s I_y/h, \quad M_{zs} = 2\sigma_s I_z/a, \tag{3.4}$$

respectively. Yield stresses of typical macroscopic materials vary from around 0.1% (aluminium and some other metals) to around 1% (paper and polymeric materials) of their Young's modulus. Some brittle materials have a yield stress much below this range, and there are special hyperelastic materials like latex, elastomeres and rubber which can have a yield stress higher than their Young's modulus.

3.2 Model by Seung *et al.*

The model described in the last section was used in the simulations of papers I, II and III. In paper IV a sheet model originally introduced by Seung [24] was used. In that model a sheet is also modeled as a triangular lattice. The lattice is connected by springs with an unstretched length a and a spring constant k [24, 37]. The corresponding energy for a pair of nearest neighbour lattice points is

$$k(x-a)^2/2 \tag{3.5}$$

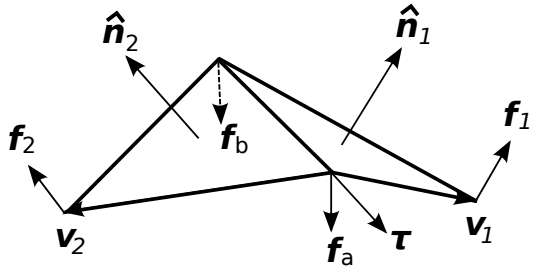

Figure 3.2: Bending of adjacent triangles. The normals $\hat{\mathbf{n}}_1$ and $\hat{\mathbf{n}}_2$ and the vectors $\mathbf{v}_1$ and $\mathbf{v}_2$ are indicated, as well as the nodal forces $\mathbf{f_a}$, $\mathbf{f_b}$, $\mathbf{f_1}$ and $\mathbf{f_2}$ resulting from bending. $\boldsymbol{\tau}$ is the bending moment.

with x the distance between the points. The sum of these energies is the in-plane energy S of the sheet. Bending rigidity is introduced by an energy cost

$$K(1 - \hat{\mathbf{n}}_1 \cdot \hat{\mathbf{n}}_2) \tag{3.6}$$

for each pair of adjacent triangles with normals $\hat{\mathbf{n}}_1$ and $\hat{\mathbf{n}}_2$, see figure 3.2. The energy corresponds to a bending moment,

$$\boldsymbol{\tau} = K\left(\hat{\mathbf{n}}_1 \times \hat{\mathbf{n}}_2\right), \tag{3.7}$$

which is balanced by forces on the four nodes of the pair. The forces $\mathbf{f}_1$ and $\mathbf{f}_2$ on the two opposing corners are given as

$$\begin{aligned} \mathbf{f}_1 &= \left(\boldsymbol{\tau} \times \mathbf{v}_1\right)/r_1^2, \\ \mathbf{f}_2 &= -\left(\boldsymbol{\tau} \times \mathbf{v}_2\right)/r_2^2. \end{aligned} \tag{3.8}$$

Here $\mathbf{v}_1$ and $\mathbf{v}_2$ are the vectors pointing from the first middle node to the corner nodes, and r_1 and r_2 are the distances of the corners from the middle edge. The forces on the middle nodes are found by requiring vanishing net moment and force for the system of adjacent triangles. We thus obtain

$$\begin{aligned} \mathbf{f}_a &= -\left[\mathbf{f}_1(1 - s_1) + \mathbf{f}_2(1 - s_2)\right]/2 \\ \mathbf{f}_b &= -\left[\mathbf{f}_1 s_1 + \mathbf{f}_2 s_2\right]/2, \end{aligned} \tag{3.9}$$

where s_1 and s_2 are the normalized components of $\mathbf{v}_1$ and $\mathbf{v}_2$ parallel to the middle edge.

In the continuum limit and with small strains this model has been shown to behave as a sheet of isotropic elastic material with thickness $h = 2\sqrt{2}\sqrt{K/k}$ and bending modulus $\kappa = K\sqrt{3}/2$ [24]. A notable difference in this model in comparison with the beam model described above is that lattice points have only translational degrees of freedom. Otherwise, the equations of motion are solved in a similar way in both models (see below). We found that these two models behave very similarly in crumpling simulations. The largest differencies in the respective elastic energies during the crumpling process were about thirty percent.

3.3 Self-avoidance

Self-avoidance of the sheet is implemented by geometrical collision tests. Self-avoidance without irregularities can be provided for a triangular lattice by resolving pairwise point-triangle contacts and edge-edge contacts [56, 14] (these geometrical primitives are indicated in figure 3.1). If a point is closer than h to a triangle, it then feels a repulsive force $\mathbf{f}_p$ normal to the triangle, as illustrated in figure 3.3a. The magnitude of $\mathbf{f}_p$ is proportional to the Young's modulus Y and the depth of the contact. Opposite forces

$$\mathbf{f}_{t1} = -w_1\mathbf{f}_p, \quad \mathbf{f}_{t2} = -w_2\mathbf{f}_p, \quad \mathbf{f}_{t3} = -w_3\mathbf{f}_p \tag{3.10}$$

are exerted on the corner points of the triangle. Here w_1, w_2 and w_3 are the barycentric coordinates of the contact point at the triangle. Edge-edge contacts are treated in a fashion similar to that of point-triangle contacts, see figure 3.3b. Here an edge means a segment between any two neighbouring lattice points.

The number of expensive pairwise contact tests described above is first pruned by a coarse proximity detection that is based on spatial partitioning with a uniform grid [14]. By this technique the number of pairwise tests is reduced to be of the order of the number of lattice points (or sheet area). Implementation of contact tests related to self-avoidance involve a fair amount of basic vector algebra. For details and related algorithms see references [56] and [14]. Friction or adhesion for sheet-sheet contacts can be applied simultaneously with self-avoidance.

An alternative approach to self-avoidance is to have impenetrable elastic spheres at the lattice points. This previously widely used approach is very fast in the implementation, but it causes uncontrolled effective friction for sheet-sheet contacts. That

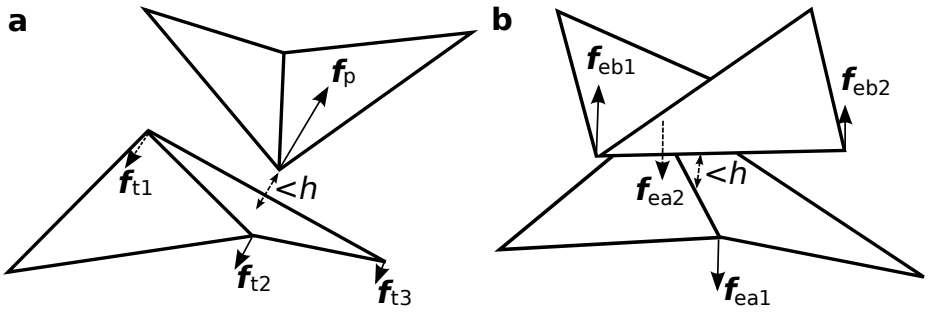

Figure 3.3: The two contact cases, a point-triangle contact (**a**) and edge-edge contact (**b**), for a triangular lattice. The triangle pairs shown represent parts of the lattice. In **a** a point closer than h to a triangle is given a repulsive force $\mathbf{f_p}$, and a force of the same magnitude but in the opposite direction is interpolated for the nodes t1, t2 and t3 of the triangle. In **b** an edge in contact with another one is given a repulsive force that is interpolated to its two nodes, ea1 and ea2. Consequently, a force of opposite direction is exerted on the other edge.

would restrict deformations of a sheet, most noticeably in the case of adhesive sheets crumpled at zero temperature. For non-adhesive sheets or in the presence of thermal fluctuations the effect does not seem to be too significant. In this approach to self-avoidance the thickness of the sheet is restricted to be equal to the lattice constant.

3.4 Langevin dynamics

Langevin dynamics is a stochastic alternative to Newtonian dynamics [10]. It adds friction and random forces to the external and interparticle systematic forces with the physical motivation of representing a simple heat bath provided by molecular collisions for coarse grained particles. The continuous form of the Langevin equation is given as

$$m\ddot{\mathbf{x}}(t) = -\nabla E(\mathbf{x}(t)) - \gamma m\dot{\mathbf{x}}(t) + \mathbf{R}(t), \tag{3.11}$$

where m is the particle mass, $\mathbf{x}$ its position, $-\nabla E$ the elastic force, and γ the collision parameter in reciprocal units of time, also known as the damping constant. The random force vector $\mathbf{R}$ is a stationary Gaussian process with statistical properties given by

$$\langle \mathbf{R}(t) \rangle = 0, \quad \left\langle \mathbf{R}(t)\mathbf{R}(t')^{\mathrm{T}} \right\rangle = 2\gamma k_B T m \delta(t - t'), \tag{3.12}$$

where k_B is the Boltzmann constant, T the target temperature, and δ the usual Dirac delta function.

The magnitude of γ determines the relative strength of the inertial forces with respect to the random forces. Connection of γ to viscosity η of the implicit solvent is provided by Stokes' law:

$$\gamma = 3\pi\eta d/m, \tag{3.13}$$

where d is the particle diameter. Increasing γ changes the dynamics of the system from an inertial to a diffusive regime. A small value for γ should be chosen if the aim is to use Langevin dynamics only to control the temperature. The time scale of the simulation should still be much longer than γ^{-1} as the equilibrium kinetic energy distribution is reached in a time $\approx \gamma^{-1}$.

When the Langevin dynamics is implemented a homogeneous distribution of random numbers can be used instead of a Gaussian one to produce the force $\mathbf{R}$, taken that the properties of equation (3.12) hold. The Dirac delta function of equation (3.11) is discretized by replacing $\delta(t - t')$ by $\delta_{nm}/\Delta t$ with Δt the simulation time step.

3.5 Solving the equations of motion

Finally, the equations of motion, whether Newtonian or Langevin, are solved for the lattice nodes by an explicit scheme [13],

$$\mathbf{v}(t+\Delta t) = \mathbf{v}(t) + \frac{\mathbf{F}}{m}\Delta t, \tag{3.14}$$

$$\boldsymbol{\omega}(t+\Delta t) = \boldsymbol{\omega}(t) + \frac{\mathbf{M}}{I}\Delta t, \tag{3.15}$$

$$\mathbf{x}(t+\Delta t) = \mathbf{x}(t) + \mathbf{v}(t+\Delta t)\Delta t. \tag{3.16}$$

Here $\mathbf{v}$ is the velocity of the lattice node, $\boldsymbol{\omega}$ its angular velocity, $\mathbf{x}$ its position and $\mathbf{F}$ and $\mathbf{M}$ the total force and moment acting on the node. More complicated higher order schemes would not necessarily provide an advantage as velocity dependent forces are relevant. Angular velocities $\boldsymbol{\omega}$ are solved for updating the orientation and deformation of the beam elements. Equation (3.15) is omitted if only translational degrees of freedom are present, as in the Seung model. The time step Δt is set by the stiffness, mass and lattice constant such that $\Delta t \approx \frac{1}{2}\sqrt{\frac{m}{aY}}$. Simulations at a high temperature or with strong attractive forces require shorter timesteps. The simulations presented in this work typically took a few million time steps.

3.6 Parallelization

Our implementations of the sheet models are parallelized by dividing the lattice into strips which are then assigned to processes (particle partitioning). This approach provides good load balancing, but a complicated part is the inter-process transfer of the lattice points that are, or are likely to be, involved in sheet-sheet contacts. In contrast with this, by using a spatial partitioning technique typical in molecular dynamics [11], self-avoidance would be easier to treat, but the tricky part would then be load balancing as the sheet fills the space very inhomogeneously in the early phases of crumpling. An overview of the implementation is given below.

At each time step the data (positions and velocities) required to handle local connectivity at the strip boundaries are exchanged with the adjacent processes. As mentioned above, in addition to this trivial part, self-avoiding contacts may require communication between any two processes. This communication is based on lists which contain the indexes of the lattice nodes whose data need to be sent or received. Each process has such lists for every other process. These lists are updated simultaneously with an update of pairwise proximity lists. In order to generate the proximity lists, positions of all lattice nodes of the sheet are gathered for each process. The send and receive

lists are then generated at each process based on these global proximity lists. It is not necessary to do this expensive operation at every time step but only when the maximum displacement of the sheet after the last update exceeds a half of the specified skin width (only the lattice nodes involved in the point-triangle or edge-edge pairs with a distance less than the skin width are included in the proximity lists). The practical skin width is a half of the thickness of the sheet.

4 Crumpling of elastic and elasto-plastic sheets

4.1 Simulation of a single ridge

As mentioned in the last chapter, previous theoretical results indicate that in the limit of large width to thickness ratio (X/h) the energy of a single elastic ridge is proportional to $\kappa(X/h)^{1/3}\phi^{7/3}$ [37], where ϕ is the bending angle of the ridge. We simulated the energy of a single ridge as a function of its size X (fixed h) for both elastic and elasto-plastic sheets (see figure 4.1). In elastic sheets the expected scaling was apparent even for fairly short ridges (the range of ridge lengths studied was chosen to represent ridge lengths that appear in simulated crumpled sheets). The energy of a ridge in an elasto-plastic sheet approached that of an elastic case as X was increased, and became nearly proportional to $(X/h)^{1/3}$, but only for clearly longer ridges than in the elastic case. The explicit ridge energies also approached $E \approx \kappa(X/h)^{1/3}\phi^{7/3}$ in agreement with previous numerical results [47, 50]. It is evident that in long enough ridges the plastic deformations are concentrated in small areas in the vicinities of vertices as suggested in reference [68], and that the elastic part of the energy dominates the deformation energy in this limit. Such a validity of the elastic theory for elasto-plastic vertices has also been shown experimentally [54].

We also tested if simulations can produce the predicted $B/S = 5$ ratio for the bending and stretching energies [68]. Our simulation model based on 3D beam elements does not explicitly deal with separate bending and stretching deformations, but the sum of all energy components related to deformations parallel to the tangent plane of the sheet gives an approximation for S, and similarly the sum of energy components related to deformations normal to the sheet approximates B. For the ridge lengths simulated (figure 4.1) we observed that $B/S > 5$, but for the longest ridges ($X/h \approx 1100$) the ratio was close to the expected value ($\approx$6.3 for the elastic ridge and $\approx$5.8 for the elasto-plastic ridge). For the elasto-plastic ridges the ratio was always slightly smaller than for the elastic ones. We determined also the magnitude of energy focusing in a single elastic ridge. The result (figure 4.2) was in agreement with the prediction that the area fraction of the sheet in which the energy density exceeds a given value ϵ should scale as $\sim \epsilon^{-5/4}$ [51, 68]. We may conclude that the model correctly describes the known scaling behavior and energy focusing in fully elastic sheets, and seems to extend such behaviour into elasto-plastic sheets in a reliable manner.

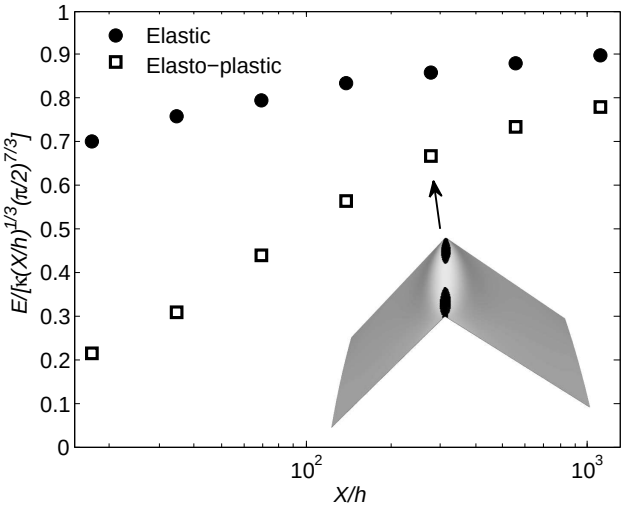

Figure 4.1: Deformation energy of a single ridge in an elastic and elasto-plastic sheet ($\sigma_y/Y = 0.01$) as a function of its length X. To form a ridge, two opposing sides of a sheet were bent to an angle of $\phi = \pi/2$. An example of a ridge in an elasto-plastic sheet is also shown, in which the areas containing plastic yielding are marked with dark shading. The energies are scaled by the expected scaling for an elastic ridge, $E \sim \kappa(X/h)^{1/3}\phi^{7/3}$ [40]. The sheet sizes were X x $4X/\sqrt{3}$.

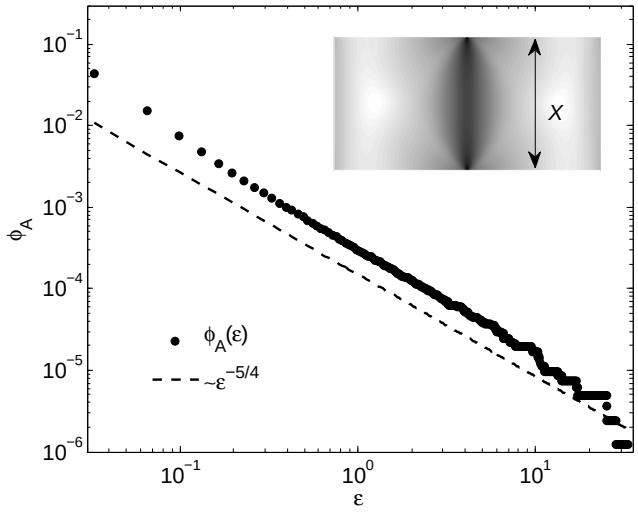

Figure 4.2: Focusing of deformation energy in an elastic ridge ($X/h \approx 1100$, the lattice size was 1280 x 640). The fraction $\phi_A(\epsilon)$ of the sheet area in which the deformation energy density exceeds ϵ is compared to the expected [51, 68] scaling $\phi_A \sim \epsilon^{-5/4}$. The energy density of the sheet is shown logarithmically shaded in the inset.

4.2 Features and energetics of forced crumpling

To simulate crumpling of thin sheets a rectangular sheet of width L was placed inside a spherical shell of decreasing radius R. The initial radius enclosing the flat sheet

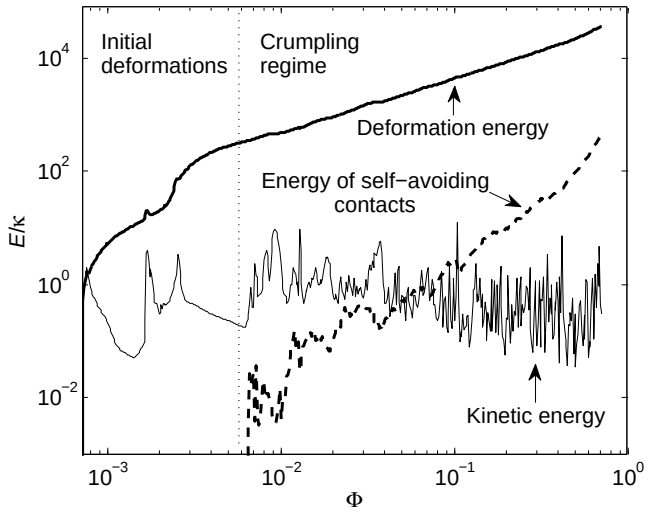

Figure 4.3: The total deformation energy, energy of self-avoiding contacts and kinetic energy as a function of solid volume fraction Φ during crumpling of an elastic sheet. The dashed vertical line indicates the location where the first sheet-sheet contacts appear.

was $R_0 \sim L$. Perturbations to the initial configurations were introduced by random variations in the initial height coordinate at each lattice site. Random forces applied on the corners of the sheet were also tested for this purpose without qualitative changes in the results. Crumpling was performed slowly so that the related inertia is assumed negligible. The simulations here consider ideal fully elastic and elasto-plastic sheets without thermal fluctuations (*i.e.* macroscopic sheets).

The external work performed by the shrinking shell that causes the crumpling in the simulations can be divided into four parts: intrinsic deformation of the sheet (technically the deformation energy of the beam elements), sheet-sheet contacts, kinetic energy and dissipation (technically the damping of the elements). The first three of these energies, during a typical simulation of crumpling of an elastic sheet, are shown in figure 4.3. It is evident that most of the energy is contained in the intrinsic deformations of the sheet. The energy of sheet-sheet contacts grows fast with increasing compression, but remains however small compared to the total deformation energy, although these contacts have an otherwise significant role in crumpling [63, 64]. The kinetic energy fluctuates heavily during the process, owing to the occational bucklings of ridges [50] and facets under tension. Such buckling causes crackling noise which has been observed to occur generally during crumpling [38, 39]. In the rest of this section we explore in more detail how fully elastic sheets crumple and then see how that is affected by plasticity.

Elastic sheets under crumpling display efficient packing in terms of energy, which is explained by the ability of the sheet to relax its shape so as to minimize its energy

during the process. Elastic sheets under compression first transform into a cone (figure 4.4a), and under further compression they display more or less symmetric folding resulting in efficiently packed configurations. An example of an efficiently packed sheet is shown in figure 4.5. In this case the sheet has reduced its energy by a series of successive symmetric foldings. Such a folded sheet apparently has a small configurational entropy, and the process is nearly deterministic. However, not all elastic sheets displayed as strong a folding as the one in figure 4.5, and at high compressions the induced packing appeared rather random.

Most of the energy of crumpled configurations is stored in the ridges between vertices. This suggests that the energy can be expressed in terms of a typical ridge length $\bar{X}$ and the energy of a single ridge. By assuming that $\bar{X} \approx L(R/L)^{\alpha}$ we can express the number of ridges as $N_X \approx (L/\bar{X})^2 \approx (L/R)^{2\alpha}$. By multiplying N_X by the scaling form for the energy of a single ridge, $E_X \sim \kappa(X/h)^{\beta} \sim \kappa(L/h)^{\beta}(R/L)^{\alpha\beta}$, we find that the

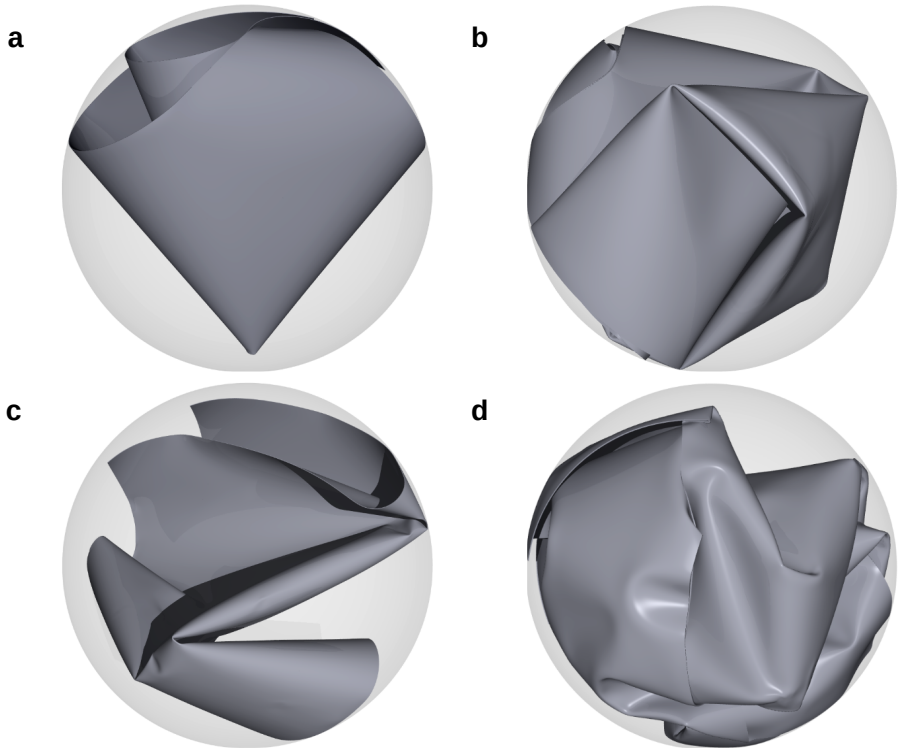

Figure 4.4: Crumpling thin sheets inside a spherical shell. An elastic sheet takes the form of a cone at radius $R = 0.44R_0$ (**a**) and has only few vertices at $R = 0.25R_0$ (**b**), while an elasto-plastic sheet (**c** and **d**) does not display a single cone regime nor elastic relaxation under crumpling and appears thus stiffer. In **c** $R = 0.44R_0$ and in **d** $R = 0.25R_0$.

total deformation energy scales as

$$E_t \sim \kappa \left(\frac{L}{h}\right)^{\beta} \left(\frac{R}{L}\right)^{\alpha(\beta-2)} . \tag{4.1}$$

An equivalent scaling relation can also be derived by dimensional analysis [63].

From simulations on elastic sheets we find that $\alpha_{el} \approx 1.65$ for $R < 0.4R_0$ (figure 4.6a). We approximated the characteristic facet size (equals approximately the typical ridge size) as a mean path of uniform sign of mean curvature when traversed along the sheet in directions parallel to its edges. With $\alpha = 1.65$ and $\beta = 1/3$, equation (4.1) gives $E_t^{el} \sim R^{-2.76}$ for elastic sheets, which is within error bars the same as our direct numerical result for the energy, $E_t^{el} \sim R^{-2.83\pm0.11}$ (figure 4.6b). This scaling law holds for volume fractions up to about 30%. Beyond this limit energy increases faster as the sheet becomes so densely packed that further folding is blocked. In elastic sheets ridge patterns at constant R/R_0 were found to be similar independent of sheet thickness.

In the case of elasto-plastic sheets the crumpling process is partly different. In vertices in particular, plastic deformations appear already in the beginning of compression. An elasto-plastic sheet is not able to transform into a cone necessary for folding type of initial deformations, as is evident from figure 4.4. As a result crumpled elasto-plastic sheets have a higher density of ridges and they appear more random than their elastic counterparts (see figure 4.7). This also becomes increasingly pronounced for an increasing width to thickness ratio L/h. For a qualitative picture of the effect of elasto-plasticity, see also figure 4.8, where ridge patterns of crumpled elastic and elasto-plastic sheets are compared.

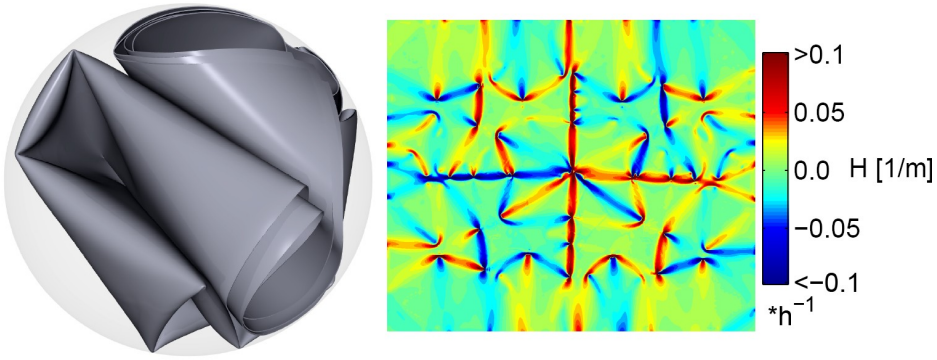

Figure 4.5: Folding inside a spherical shell. Snapshot on the left shows the membrane in a symmetrically folded configuration. A colour coded mean curvature map on the right displays the symmetrical fold pattern of the configuration. The mean curvature was extracted from the simulation lattice using equation (2.13). The width to thickness ratio of the membrane is 1000 : 1, and the radius of the crumpled configuration is $R = 0.25R_0$.

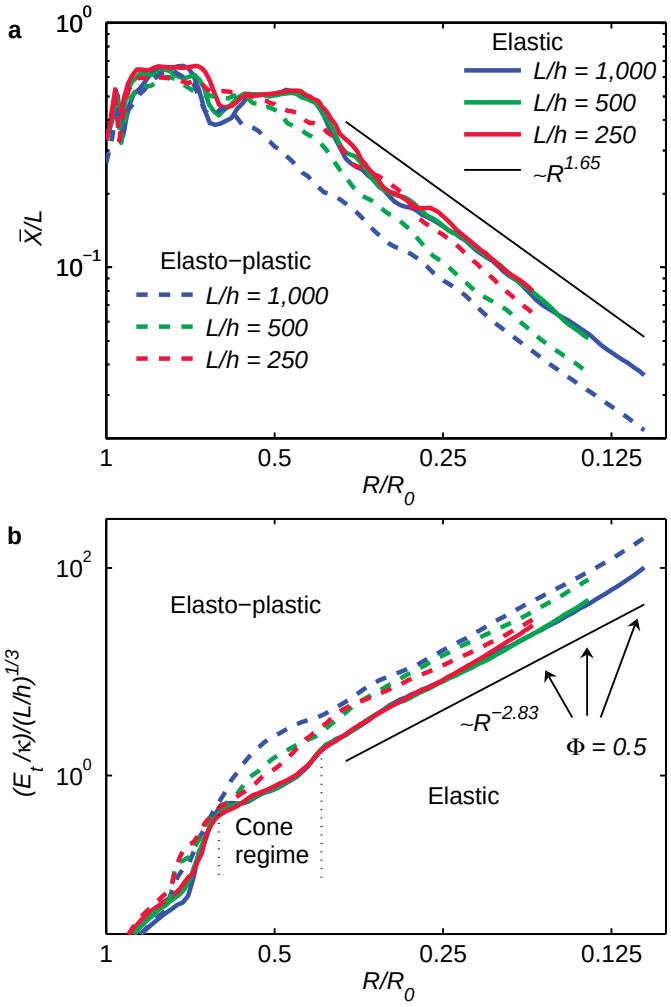

Figure 4.6: Development of facet size and deformation energy during crumpling. **a**, Average linear size of areas with uniform sign of mean curvature for elastic and elasto-plastic sheets of size $L/h = 250$, 500 and 1000. In a crumpled state ($R < 0.4R_0$) this size describes the characteristic size of facets and ridges in the sheet. **b**, The total energy of elastic and elasto-plastic sheets of size $L/h = 250$, 500 and 1000, scaled by $1/(L/h)^{1/3}$. Transitions in the energy of the elastic sheets at $R \approx 0.75R_0$ and $R \approx 0.4R_0$ indicate the formation of a cone and the end of a single-cone regime, respectively. The plots shown are averages of three simulations, and the yield point of the elasto-plastic sheets is $\sigma_y/Y = 0.01$.

It is evident from figure 4.6 that for small R/R_0 the average facet size and energy of elasto-plastic sheets scale similarly as a function of compression to the elastic sheets. However, the relative facet diameter decreases for increasing L/h, and consequently, the scaled energy increases with L/h. This also means that similarity of ridge patterns at constant R/R_0 found for crumpled elastic sheets does not hold for elasto-plastic sheets.

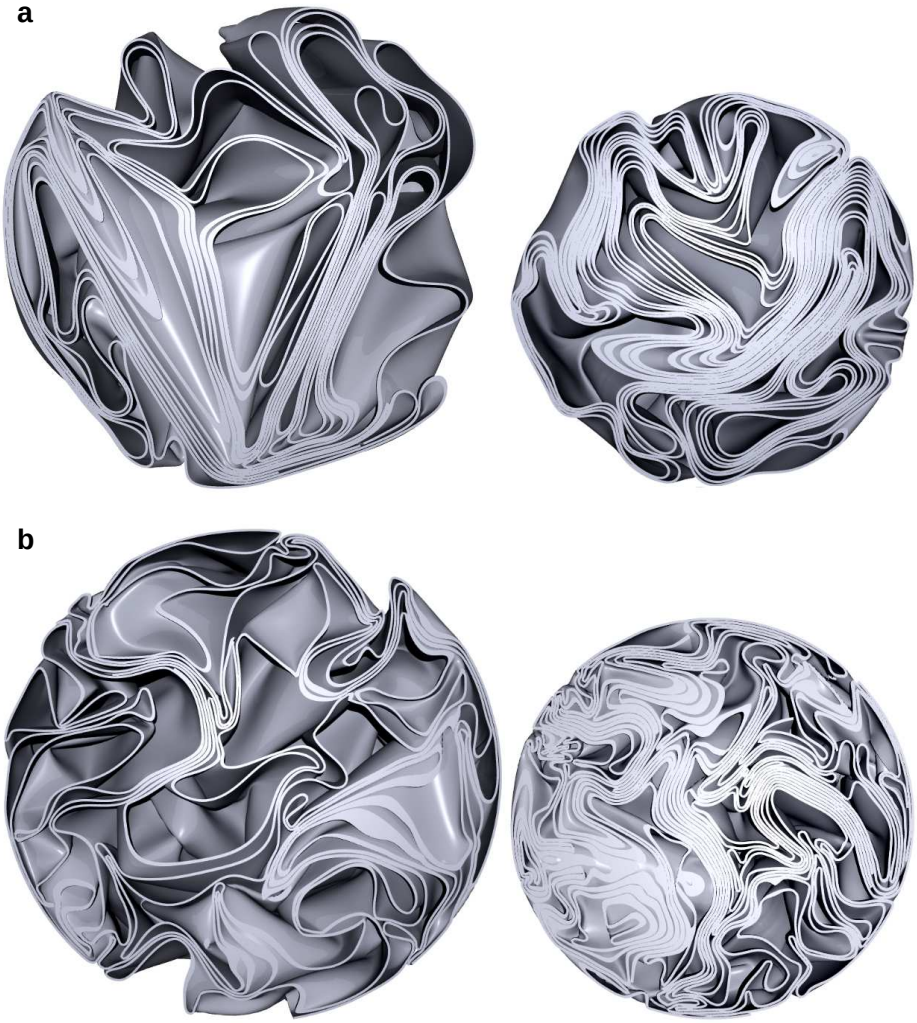

Figure 4.7: Intersections of crumpled sheets. Snapshots are taken at volume fractions of $\Phi = 0.25$ (left) and $\Phi = 0.5$ (right) for sheets with $L/h = 1000$. A crumpled elastic sheet (**a**) is more effectively folded, indicated by its more layered structure, so that it has a larger characteristic facet size and a lower energy than a crumpled elasto-plastic sheet (**b**). The yield stress $\sigma_s/Y = 0.01$ is typical for e.g. paper [65].

The L/h dependence in the crumpling of elasto-plastic sheets arises from the L/h dependence of deformations which involve plastic yielding. For increasing L/h the plastic fraction of energy becomes increasingly concentrated only on the tips of vertices (in agreement with simulations of a single ridge above). For small L/h the spatially more extended plasticity of vertices and ridges makes them relatively weaker. Such sheets can, to some extent, accommodate further confinement by extending the size of existing plastic deformations instead of forming new initially elastic deformations. An existing plastic vertex can then (small L/h) move so as to form a plastically deformed

crease. The length of a plastic crease cannot scale proportional to the sheet size (fixed h) because of the crease's rapidly increasing energy with increasing length. Formation of new ridges and vertices becomes preferred as L/h is increased. Elasto-plastic sheets of small width to thickness ratio may thus deform to shapes close to those of elastic sheets during their early phase of compression, and may thereby sustain a relatively higher facet size and lower energy during further crumpling in comparison with elasto-plastic sheets of higher width to thickness ratio.

We have so far only considered simulations of frictionless sheets. Adding friction is expected to hinder folding and relaxation of an elastic sheet and leading to random crumpling, higher stiffness and energy, as plasticity also does. This is qualitatively evident in figure 4.8, where crumpled frictionless sheets are compared with an elastic sheet having a friction coefficient of $\mu = 0.5$ typical of real materials. A thorough quantitative analysis of the effect of friction was not carried out within this Thesis.

4.3 Facet size distributions

It is evident by experience and by the simulations above (see e.g. figures 4.7 and 4.8) that ridges and facets in crumpled geometry are not of uniform size. To determine the facet size distributions of crumpled sheets, 2D mean curvature maps were thresholded resulting in binary images where areas of positive and negative curvature were marked respectively as black and white (figure 4.9). Black and white areas were then split into separate roughly convex regions by applying the watershed algorithm [35]. These regions approximate facets. Their relative linear sizes x were determined as square roots of their areas divided by the linear size L of the sheet. Facets with a size smaller than $L/100$ were omitted from the analysis. This procedure does not rely on any assumption regarding the detailed shape or energy content of the ridges. It is thus straightforward to apply at any degree of crumpling and in sheets of varying width to thickness ratio.

Facet size distributions in crumpled sheets were reasonably well described by a log-normal distribution

$$N(x) \sim \frac{1}{x\sigma} e^{-[ln(x)-\mu]^2/(2\sigma^2)}, \tag{4.2}$$

where μ is the mean of the distribution, see figure 4.10a. The found standard deviations $\sigma \approx 0.5$ for the logarithms of linear facet sizes correspond to $\sigma \approx 1.0$ for the facet areas in good agreement with the $\sigma \approx 1.17$ found for crumpled paper [72]. For ridge lengths l in simulated crumpled elastic sheets a lognormal distribution given in the form

$$N(l) \sim \frac{1}{\sqrt{b}l} e^{-[log(l/l_0)]^2/b} \tag{4.3}$$

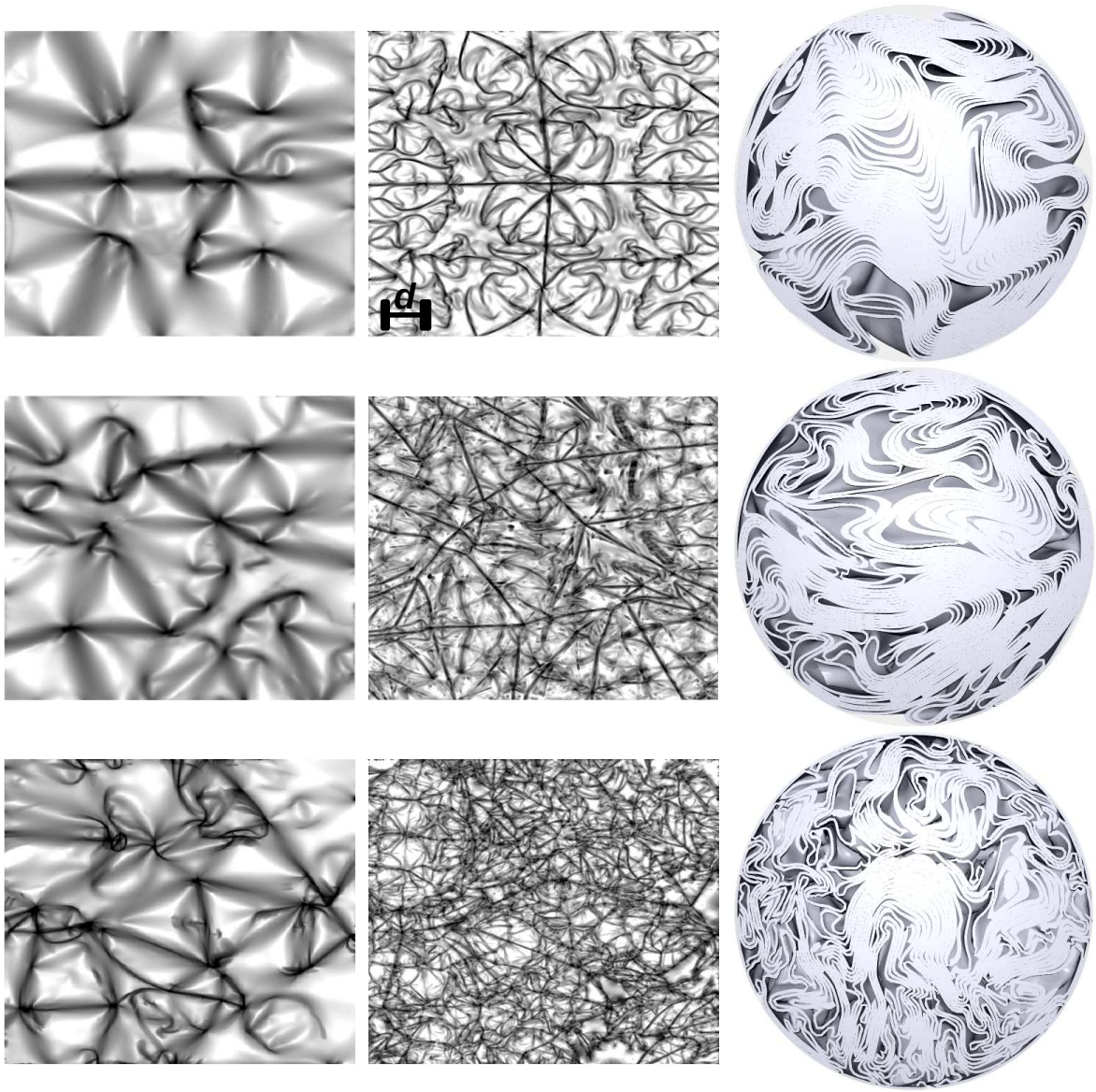

Figure 4.8: Maps of logarithmically scaled deformation energy density of a crumpled frictionless elastic sheet (top), elastic sheet with friction (middle) and frictionless elasto-plastic sheet (bottom). Maps on the left column are for mildly crumpled states (solid volume fraction $\Phi = 0.03$) and those in the middle for strongly crumpled states ($\Phi = 0.7$). The friction coefficient of the sheet in the middle row is $\mu = 0.5$, and the yield stress of the elasto-plastic sheet is $\sigma_y/Y = 0.01$. Cross-sections in the right column display the structures of the strongly crumpled states. The diameter d of the confining spheres is marked in the topmost energy density map of the middle column.

has earlier been found with $b = 0.95$ [63]. This corresponds to $\sigma \approx 0.7$, and is also in agreement with the present results. The lognormal distribution found for the ridge lengths in crumpled paper [60] is a bit wider ($\sigma \approx 1.2 - 1.4$). A wider ridge length

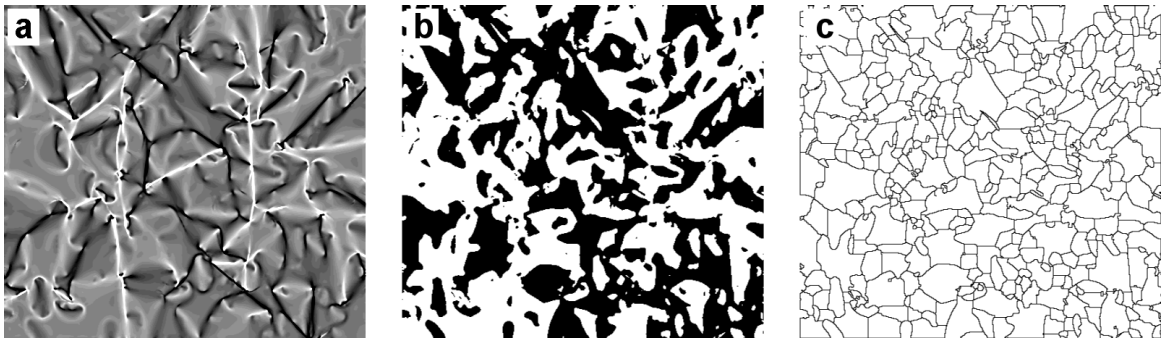

Figure 4.9: Illustration of facet segmentation. **a**, Mean curvature field of a crumpled sheet. **b**, Thresholded areas of positive (white) and negative (black) curvature. **c**, The thresholded image segmented into regions which approximate facets.

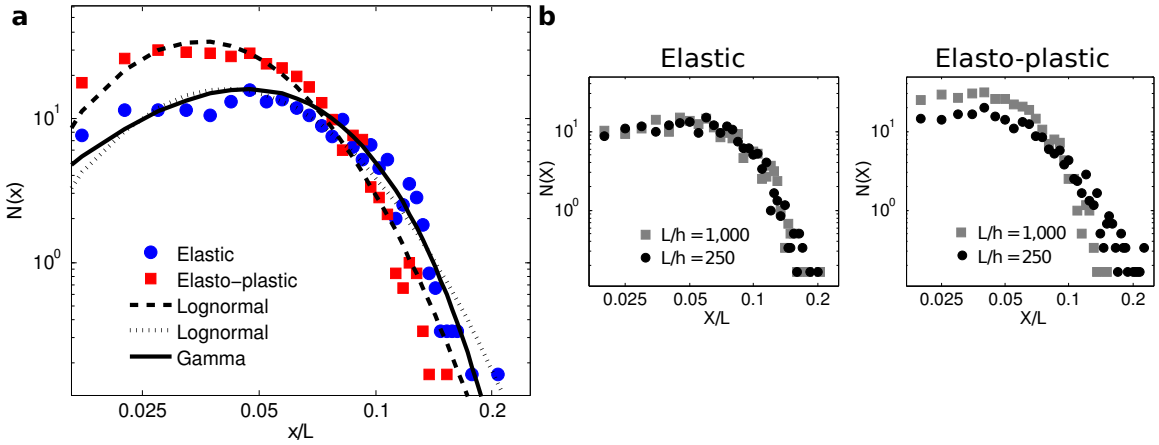

Figure 4.10: **a**, Distributions of relative linear facet size x are shown for elasto-plastic (yield stress $\sigma_y = 0.01Y$) and elastic sheets of size $L/h = 1000$. The parameters of the lognormal distribution fit (see text) for elastic sheets are $\mu = -2.90$ and $\sigma = 0.52$ and for elasto-plastic sheets they are $\mu = -3.15$ and $\sigma = 0.47$. The parameters of the gamma distribution fit for elastic sheets are $a = 4.0$ and $b = 0.015$. **b**, Comparison of facet size distributions for $L/h = 250$ and $L/h = 1000$. Distributions in **a** and **b** are averages over those for six sheets crumpled to $R/R_0 = 0.18$.

distribution may arise from the fact that a single facet is surrounded by multiple ridges of varying length. The lognormal distribution suggests a mechanism in which facets and ridges break into smaller ones having sizes that are random fractions of the sizes of the original ones [68].

In the case of elastic sheets, a slightly better fit in comparison with a lognormal fit was provided by a gamma distribution

$$N(x) \sim \frac{x^{a-1}}{b^a \Gamma(a)} e^{-x/b} \tag{4.4}$$

with the shape parameter $a = 4.0$ (figure 4.10a). The scale of the distribution is given

by b. A gamma distribution has previously been found for the segment lengths of a 1D model of crumpling, owing to interaction at high confinement of segment layers [64]. Crumpled elastic sheets display a much more stronger layering than elasto-plastic sheets, and this may explain their somewhat different facet size distributions. Figure 4.10b displays the similarity of distributions of relative facet size for elastic sheets of varying L/h, while in the case of elasto-plastic sheets the distribution changes with increasing L/h such that its mean decreases.

4.4 Fractal dimension

Fractal dimension of crumpled sheets is a measure for how sheet size affects compactification, and it has been measured for sheets of different materials [23, 71, 73, 22]. The fractal dimension D relates the radii R of crumpled configurations to the linear sizes L of the sheets such that $R \sim L^{2/D}$, or equivalently $L^2 \sim R^D \sim M$. To achieve this relation for forced crumpling, one needs also to define a condition for when the crumpled radii R are measured. A usual practice is to measure R when a predefined compressive force is reached. A value D close to its lower physical limit, $D = 2$, means a loose 'packing' of the crumpled sheet and that much force is required for crumpling of large sheets. On the other hand, a value of D close its upper physical limit, $D = 3$, means that a compact structure results from application of much less force. A natural assumption is that D is determined by the density of vertices, facets and ridges, and by the scaling of the energies of these structures with their size.

We can derive a scaling expression for the fractal dimension of crumpled elastic sheets by considering the dependence of their energy on their size R, and determining the point at which a predefined total force $F \approx dE/dR = const$ is reached. Inserting a constant force in equation (4.1), and expressing it in the form $R(L)$, the fractal dimension defined by $R \sim L^{2/D_{el}}$ can be found such that

$$D_{el} = 2 + \frac{2(1-\beta)}{(2-\beta)\alpha + \beta}. \tag{4.5}$$

Similarity of elastic ridge patterns thus leads to the result that the fractal dimension of crumpled elastic sheets only depends on the scaling properties under crumpling of the average ridge length and ridge energy. Using the numerically obtained values for these scaling properties, $\alpha_{el} \simeq 1.65$ and $\beta_{el} \simeq 0.33$, equation (4.5) gives $D_{el} \simeq 2.43$.

In elasto-plastic sheets the lack of similarity of ridge patterns means that there is an additional L/h dependence in the average ridge length, which would appear in an equation for the total elastic energy of the ridges similar otherwise to equation (4.1) (the exponent in the L/h term would effectively be increased), and thereby in a subsequent expression for the fractal dimension. We do not attempt to derive such

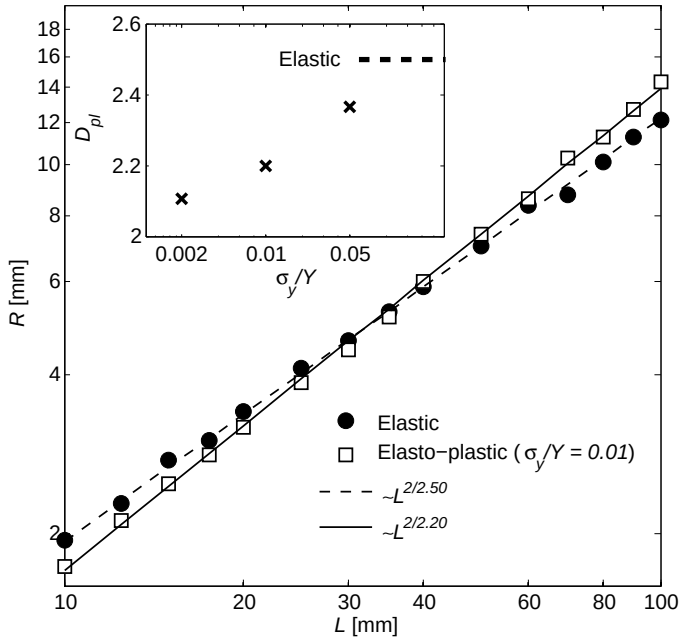

Figure 4.11: Relation of sheet width to the final radius of the crumpled configuration. Sheets of varying size (fixed h) were crumpled until the confining force reached 50 N. Scaling fits to simulated final radii as a function of L indicate a fractal dimension of $D_{el} = 2.50 \pm 0.03$ for elastic sheets and $D_{pl} = 2.20 \pm 0.03$ for elasto-plastic sheets with the yield point $\sigma_y/Y = 0.01$. The plots shown are averages over three simulations. Fractal dimensions for different yield points are shown in the inset.

an expression here, but can however draw some conclusions concerning the fractal dimension in the elasto-plastic case. Since the ridge density will in this case increase with increasing sheet size, the energy and 'strength' of crumpled elasto-plastic sheets will increase faster with increasing sheet size than in the elastic case (at the same time the energy to create a single ridge approaches that of an elastic ridge). The fractal dimension of elasto-plastic sheets, D_{pl}, must thus be smaller than the D_{el} of equation (4.5). This conclusion follows also from equation (4.5) if the exponent in the L/h term in equation (4.1) is increased.

In order to obtain numerical values for the fractal dimensions, we crumpled elastic and elasto-plastic sheets of size varying from 1 cm^2 to 100 cm^2. The thickness of the sheets was 0.1 mm and their Young's modulus was 1 GPa. A predefined force of 50 N was chosen, and the plastic yield stress was $\sigma_y/Y = 0.002, 0.01$ or 0.05. For elastic sheets we found $D_{el} \simeq 2.50$ in excellent agreement with the scaling result above, and in elasto-plastic sheets D_{pl} increased from about 2.11 to about 2.37 for increasing values of σ_y, also very much as expected (see figure 4.11). When the compression force was increased, we observed a slight increase in the fractal dimensions. This is reasonable since in the limit of high compression $D = 3$.

5 Fluctuating adhesive membranes

5.1 Membranes with attractive interaction

Attractive Van der Waals interactions are essential for conformations of polymers and membranes at nanometer scales [8], while such forces can largely be neglected in their macroscopic counterparts. Attraction forces and fluctuations induce a tendency for 1D and 2D nano-structures to collapse spontaneously as long as they are free to deform in a 3D space. Microscopic membranes in particular have a large surface area and may thus easily minimize their potential energy by forming conformations with large contact areas. Examples of such membranes include, e.g., graphene [61, 67, 74], graphitic oxide membranes [34], recently synthetized nanoparticle membranes [80], polymerized membranes [62] and lipid bilayers (typically having cross-linked proteins embedded in them), including the skeleton of red blood cells [32]. For example, scrolled and folded graphene sheets have been observed in various experiments [57, 67].

In this chapter membranes are described by the Seung model introduced in Chapter 2. The lattice constant in the model is set to $a = 2h$. The self-avoidance and attraction of membrane-membrane contacts is implemented by proximity detection for non-nearest neighbour point-triangle pairs and for non-nearest neighbour edge-edge pairs, as described in Chapter 2. Proximity detection yields the midplane separation r and the related contact normal for any two parts of the membrane close to each other. For separations $h < r < 2h$ the two parts interact through an attractive harmonic potential which has energy $-W$ per unit area at $r = h$. Contacts with $r < h$ are penalized by a strong repulsive harmonic potential. We restrict the investigation to hexagonal fully elastic membranes which have the width to thickness ratio $L/h = 1000$ along the diagonal (see figure 5.1A). We simulate Langevin dynamics in the regime of relatively small damping, *i.e.*, the membrane is assumed to be surrounded by a dilute fluid.

A thin membrane with attractive forces can efficiently lower its potential energy by either folding or scrolling. The simplest forms of such configurations are displayed in figures 5.1B and 5.1C. Simulations demonstrate that these types of configurations often appear if strong fluctuations or external forces have been exerted on the membrane. It is therefore of interest to investigate these structures in more detail. Their stability is determined by a balance between the elastic deformation energy E_{el} and

the potential energy of the attraction force E_A.

Consider a square membrane of linear size L (the same analysis applies for hexagonal membranes used in the simulations), which is folded once so that a smooth loop of length l is formed at the end of the fold, as in figure 5.1C. We recall the elastic energy $E_{el} = a\kappa L/l$ with $a \approx 18.33$ of such a loop from equation (2.21). The size of the adhered part of the fold is $L(L-l)/2$, which means that the total energy of the fold is given by

$$E_f = E_{el} + E_A = a\kappa L/l - WL(L-l)/2. \tag{5.1}$$

E_f has a minimum at $l = \sqrt{2a\kappa/W}$. If $L > L_f^* = 2\sqrt{2a\kappa/W}$ the fold is stable, *i.e.*, it has a smaller energy than a flat membrane ($E = 0$).

The energy of a scrolled membrane is well approximated by a membrane with a constant curvature of radius R. The total energy of a scrolled membrane is then

$$E_r = E_{el} + E_A = \kappa L^2/2R^2 - WL(L - 2\pi R) \tag{5.2}$$

with a minimum $E_r < 0$ at $R = (\kappa L/2\pi W)^{1/3}$ if $L > L_r^* = 3\pi\sqrt{3\kappa/2W}$. The minimal membrane size for a stable scroll is almost equal to that of a fold, $L_r^* \approx L_f^* = L^*$. The fold and scroll energies are compared in figure 5.2.

An interesting question regarding adhesive membranes is whether they could undergo crumpling into a small volume without strong external compression. Figures 5.3D and 5.3E display the total energy $E = E_{el} + E_A$ and pressure P for non-adhesive ($W = 0$) and adhesive ($WL^2/\kappa = 10^4$, $L \approx 8L^*$) membranes during forced confinement at zero temperature. The pressure was determined as the areal force density the membrane exerts on the shell, and the shell radius was decreased at a constant rate. At the beginning of the compression the energies and pressures of these two cases coincide as there is no contact area. For smaller confinement radii, membrane-membrane contacts become unavoidable and the adhesive membrane folds resulting in a drop in its total energy. The first folds appear with little cost in the elastic energy, but soon compression demands more elastic energy than what is gained by creating new contact surface, and the energy begins to grow. The overall minimum in the total energy of the adhesive membranes came close to that of a scrolled membrane. Rather surprisingly, the average pressure was almost the same in the two cases. This means that the energy released through attraction force does not aid the packing of the membrane, and it mainly dissipates.

It is also useful to compare the energy $E \approx b\kappa(L/h)^{1/3}(V/V_0)^{-0.9}$ of a confined non-adhesive membrane (the constant $b \approx 3.7$, see figure 5.3D) with the maximum possible energy gain WL^2 from attraction. If V/V_0 is large enough for $WL^2 \gtrsim b\kappa(L/h)^{1/3}(V/V_0)^{-0.9}$, the packing of the membrane is expected to be dominated by the attraction forces and it has large adhered folds as in figure 5.3B. When V/V_0 is reduced, the relative energy gain of adhesion becomes weaker and the compression

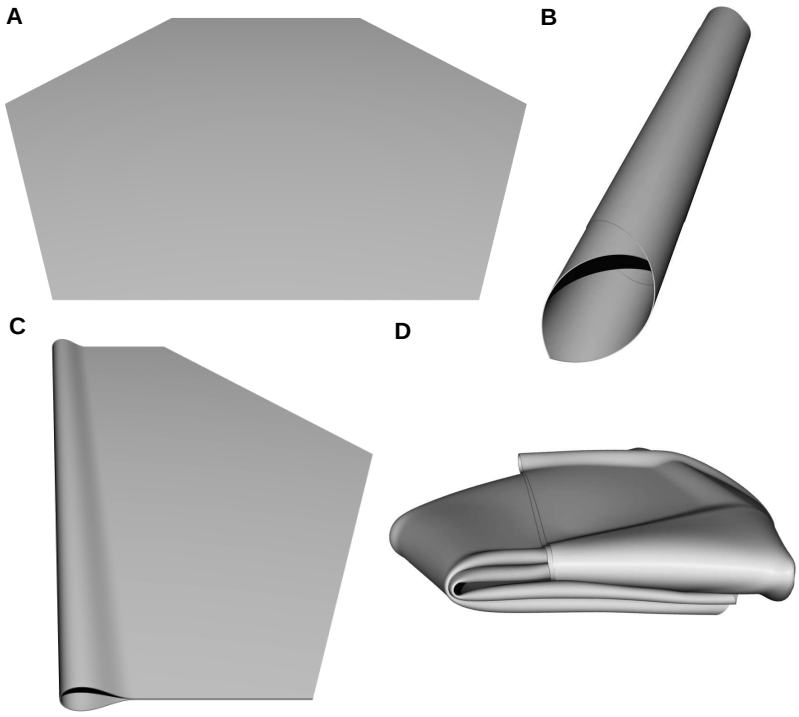

Figure 5.1: Simulated adhesive membranes in a flat (**A**), scrolled (**B**), once folded (**C**) and multiply folded collapsed (**D**) configuration. The membranes have the strength of attraction $WL^2/\kappa = 10^3$ (flat, once folded, scrolled) or $WL^2/\kappa = 10^4$ (collapsed).

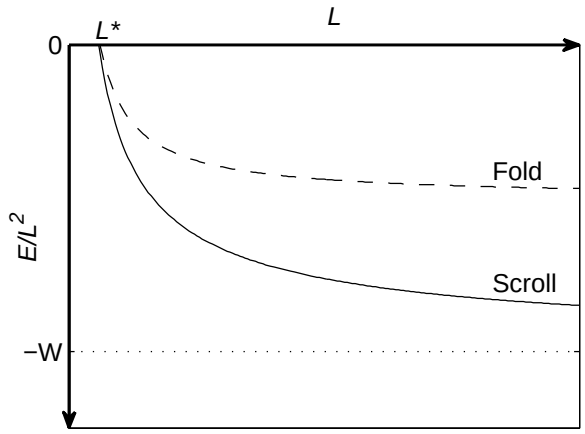

Figure 5.2: The total energy per area for once folded and scrolled membranes as a function of sheet size L. The critical size L^* is indicated, and the energies are compared to the adhesion energy density W.

will proceed like in the non-adhesive case. When this happens the folds will become elastic ridges [37]. For simulated membranes with $WL^2/\kappa = 10^4$, the total energy

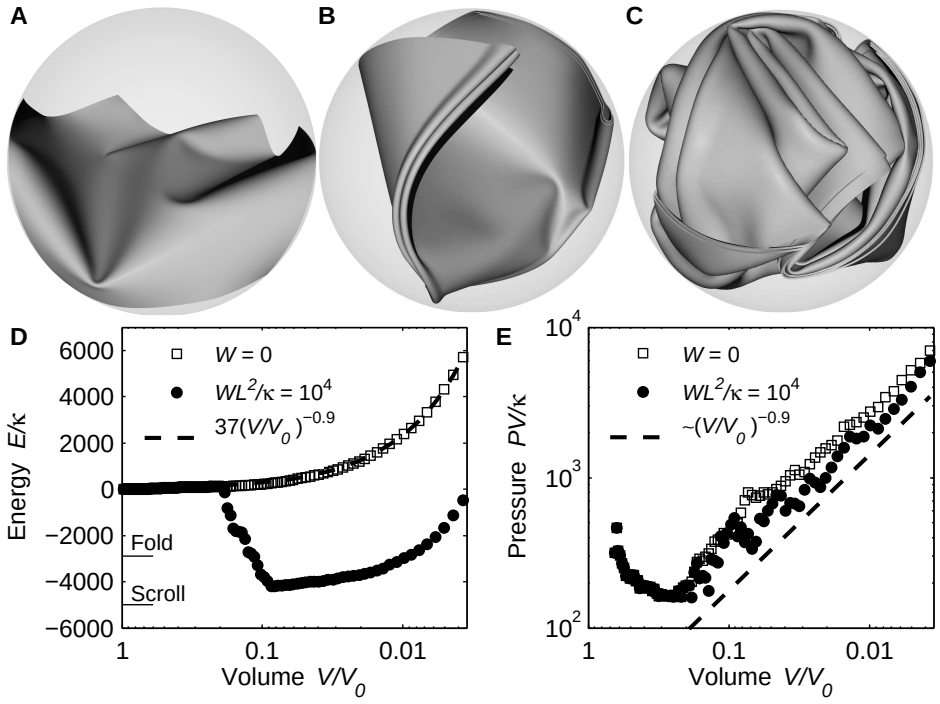

Figure 5.3: Forced crumpling of membranes. (**A**) Adhesive membrane loosely confined in a spherical shell. The volume of the shell relative to its initial volume is $V/V_0 \approx 0.5$. (**B**) The membrane twice folded at $V/V_0 \approx 0.05$. (**C**) The membrane highly compressed at $V/V_0 \approx 0.004$. (**D**) Total energy $E/\kappa = E_{el}/\kappa + E_A/\kappa$ of non-adhesive ($W = 0$) and adhesive ($WL^2/\kappa = 10^4$) membranes during compression. The energy of non-adhesive membranes is compared to $E/\kappa = 3.7(L/h)^{1/3}(V/V_0)^{-0.9} = 37(V/V_0)^{-0.9}$. The energies that would result from folding once or scrolling up an adhesive membrane are indicated by line segments. (**E**) The pressure exerted by the membranes against the confining shell during compression. The pressures are compared with $PV/\kappa \sim (V/V_0)^{-0.9}$. The plots in (**D**) and (**E**) are averages of five independent simulation runs.

$E_{el} + E_A$ turned positive at $V/V_0 \approx 0.004$. At this point the elastic energy of adhesive membranes became roughly equal to that of non-adhesive ones. The similarity of elastic energies in the two cases at high confinement reflects the fact that packing of adhesive membranes was not more efficient than that of non-adhesive ones.

When the external compression of adhesive membranes was relaxed, they opened up into multiply folded collapsed conformations, as in figure 5.1D, if the adhesion was strong ($L \gg L^*$). These collapsed conformations were fairly flat rather than spherical. Membranes with weaker adhesion opened up as folded and in some cases as scrolled configurations. The latter requires that the opposing sides of the membrane have adhered at some point. If the membrane size was less than L^*, a flat configuration always resulted when compression was released.

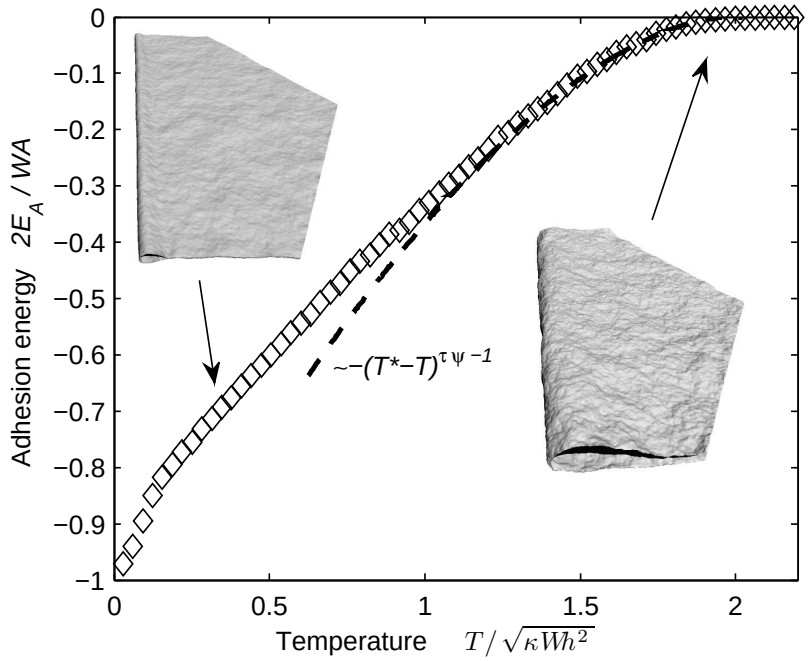

Figure 5.4: Heating of a folded adhesive membrane. The adhesion energy E_A is shown scaled by $WA/2$ with A the membrane area (open diamonds). The two snapshots show the fluctuating membrane at $T = \sqrt{\kappa W h^2}/3$ and close to the temperature at which the fold opens up completely. This temperature should approach the unbinding temperature T^* in the limit of large membrane size (here $L/h = 1000$) with sufficiently strong attractive interaction (here $WL^2/\kappa = 10^5$). In that case the adhesion energy is expected to vanish as $\sim -(T^* - T)^{\tau\psi-1}$ [28]. This scaling behaviour is plotted as a dashed line using the theoretical estimate $\tau\psi = 2.7$ [26] and $T^* = 2.0\sqrt{\kappa W h^2}$.

5.2 Role of thermal fluctuations

Perhaps the most interesting question related to the stability of microscopic membranes is whether folded, scrolled or collapsed configurations are likely to appear as a result of thermal fluctuations. If this is the case, then free standing membranes do not exist. We give temperatures here as energies by including the Boltzmann constant k_B in T.

For a stack of flat membranes bound together by attractive forces it has been shown by renormalization methods that there is a critical unbinding temperature T^* at which thermal fluctuations overcome the attraction [18, 8]. For fluid membranes $T^* \approx \sqrt{\kappa W d^2}$ [8, 29], where d is the range of attraction. For our rigid fixed connectivity membranes we found $T^* \approx 2\sqrt{\kappa W h^2}$ (we have $d = h$) by heating up a folded membrane (figure 5.4). A higher T^* in comparison with that of fluid membranes is expected due to in-plane stiffness.

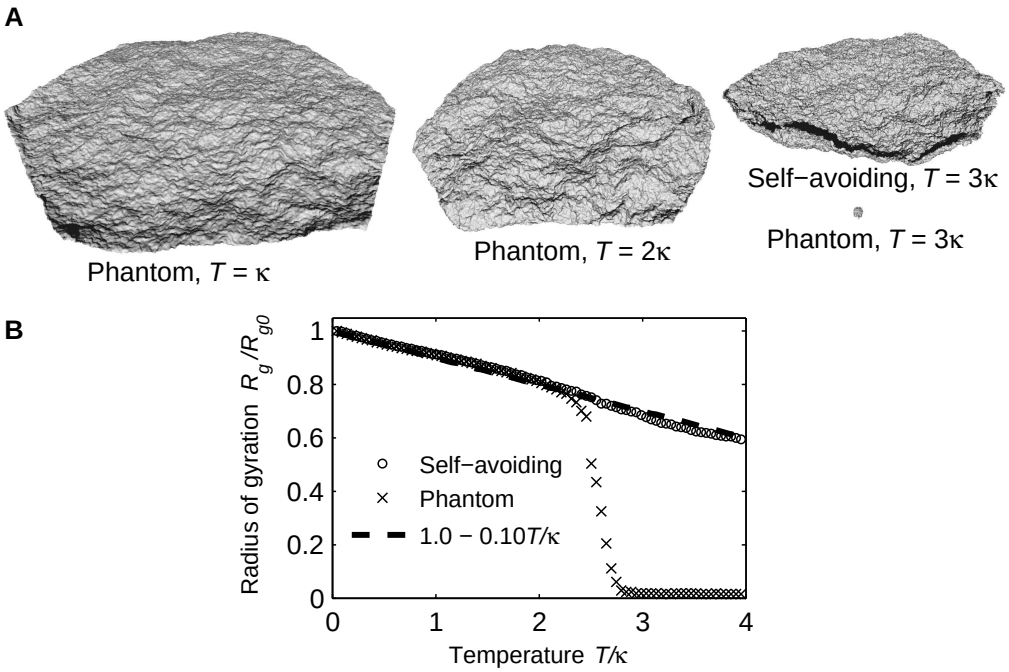

Figure 5.5: Heating of non-adhesive flat membranes. (**A**) A phantom membrane at temperatures $T = \kappa$, $T = 2\kappa$ and $T = 3\kappa$, and a self-avoiding membrane at $T = 3\kappa$. (**B**) Radius of gyration R_g (defined as $R_g^2 = \sum_{k=1}^{N} |\mathbf{r}_k - \mathbf{r}_{mean}|^2/N$, where $\mathbf{r}$ is particle position) as a function of temperature for the phantom and self-avoiding membrane divided by its zero temperature value R_{g0}. The drop in the radius of gyration of the phantom membrane indicates its collapse by crumpling, while its self-avoiding counterpart displays only linear shrinkage $R_g/R_{g0} \approx 1.0 - 0.10\ T/\kappa$. The crumpling transition temperature agrees with $T \approx 2.6\kappa$ found by earlier Monte Carlo simulations [22].

Previous simulations have demonstrated that adhesive membranes without bending stiffness ($\kappa = 0$) collapse to a folded or even compact phase below T^* [27, 28, 30, 36]. However, we argue here that in a typical experimental environment and for realistic membranes, the bending modulus κ tends to be so high that the energy of thermal fluctuations below T^* typically cannot drive the membrane to collapse. Above T^*, membranes with fixed internal connectivity are always flat [12, 48]. We confirmed the high T flatness of our membranes by heating them up to a very high temperature. By switching off self-avoidance we found crumpling at $T \approx 2.6\kappa$ in agreement with early Monte Carlo simulations [22], see figure 5.5.

The minimum energy barrier that thermal fluctuations need to overcome to collapse an adhesive membrane corresponds to the energy needed to bend a corner of the membrane around to touch itself. Making such a deformation of a hexagonal membrane used in our simulations requires an energy $E_{el} \approx 10\kappa$. This is a useful approximation for the lowest energy barrier. The temperature must then be close to 10κ to overcome the barrier, but at the same time it must be below the unbinding temperature

T^*. Consequently, for a membrane to fold spontaneously, within a feasible timescale, a rough estimate found by simulating free standing membranes ($L > L^*$) is that T must be within the interval $\sqrt{\kappa W h^2} \gtrsim T \gtrsim \kappa$. If adhesion is weak such that the unbinding temperature is much less than the bending modulus, then flatness is metastable at $T < T^*$.

Next we turn to forced compression of membranes at $T > 0$ in order to investigate whether there are any significant differences arising from thermal fluctuations. Earlier investigations have revealed that self-avoiding membranes with fixed internal connectivity do not crumple by heating, not even if a membrane has zero thickness and no explicit bending rigidity [12, 48]. In such a case the membrane could be packed into a small volume without energy, which implies that the reason for the absence of crumpling is purely entropic and that there would be a free energy cost for crumpling due to loss of entropy.

However, it is not clear whether it requires more or less external work to compress a membrane at a high temperature than at a low temperature. Entropic rigidity is likely to increase compression stiffness, but thermal fluctuations may also help the membrane to find the most efficient packing configurations. Simulations suggest, however, that this is not the case. Crumpling of a fluctuating membrane requires more external work, and heating up a compressed membrane increases the pressure that the membrane exerts against the confining shell, as is shown in figure 5.6B for non-adhesive and adhesive ($WL^2/\kappa = 2.5 \times 10^4$) membranes at the confinement $V/V_0 = 0.004$. For non-adhesive membranes we find from these simulations that there is an approximately linear increase in the pressure with increasing temperature: the pressure is approximately $P \approx P_{T=0}(1 + \alpha T/\kappa)$ with $\alpha \approx 2$. We experimented also with other degrees of compression finding always a positive α. We did not attempt to find the precise volume, membrane size or adhesion strength dependencies of the pressure within this work. The increase in pressure with temperature is analogous to the behaviour of compressed solid or fluid, but opposite to that of rubber. The pressure increase is, however, quite moderate considering that the highest simulated temperature $T = \kappa$ would be a very high temperature in an experiment.

The unbinding temperature of the compressed adhesive membranes can be seen in figure 5.6B as the point where the pressure begins to increase at an equal rate with the non-adhesive membranes. At this point ($T \approx T^* \approx 0.3\kappa$) tightly bound layers break up as a result of increased thermal fluctuations. The layers 'swell' as can be observed in figure 5.6A. The overall conformation is, however, not affected much. This is quite reasonable since confinement of an elastic membrane in a small volume results in a very efficient conformation in terms of energy already at zero temperature. In addition, such conformations consist of large ridges and folds whose energies are far beyond the simulated temperatures.

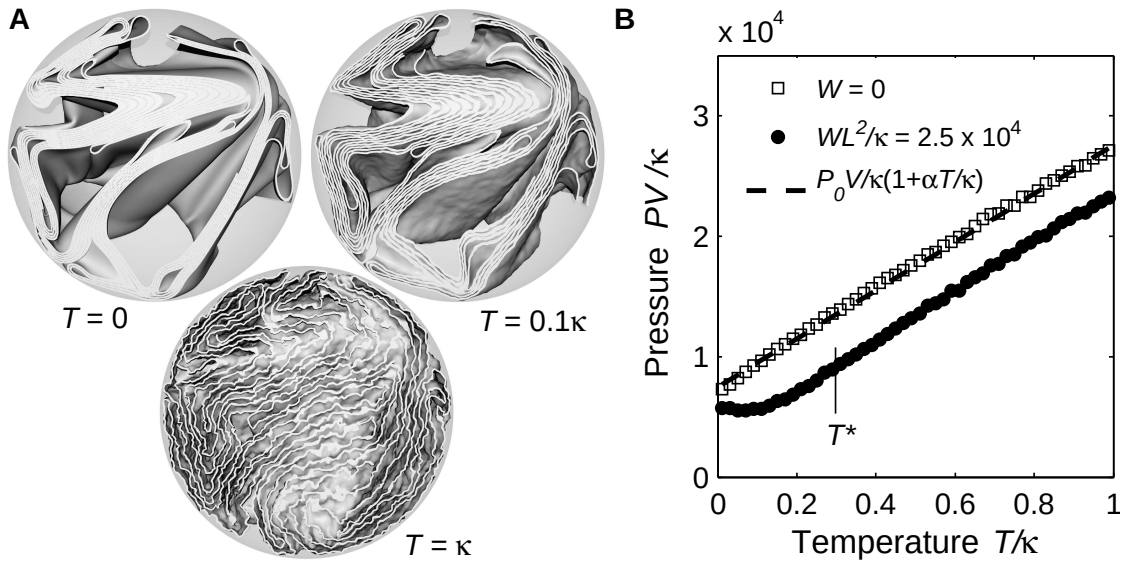

Figure 5.6: (**A**) Confined adhesive membrane ($WL^2/\kappa = 2.5\times10^4$, $T^* \approx 0.3\kappa$) at zero temperature, below the unbinding temperature ($T = 0.1\kappa$) and above it ($T = \kappa$). (**B**) Pressure exerted by non-adhesive and adhesive membrane as a function of temperature. The dashed line shows a linear fit with $\alpha = 2$. The confining volume in (**A**) and (**B**) is $V/V_0 = 0.004$.

5.3 Comparison with real membranes

We are now in a position to review properties of some real adhesive membranes and to consider applicability of our results to them. Membranes in biological systems are typically composed of phospholipid bilayers embedded with proteins [12, 8]. If the proteins form a dense cross-linked network then the membrane behaves as a solid elastic membrane studied here. A typical bending modulus for biological membranes is $\kappa \approx 0.3-0.6$ eV, but the strength of their attractive interaction varies a lot depending on their composition [8]. However, repulsive hydration forces typically result in separations by about two or three nanometers reducing the attractive van der Waals interaction [12]. The regime $W > 10^{-6}$ J/m^2 has been characterized as a regime of 'strong' adhesion for lipid bilayer vesicles [66]. A membrane with $W = 10^{-6}$ J/m^2 would have $L^* \approx 3-4$ μm, such that for a membrane size of the order of a few micrometers the conformations could be affected by adhesion in the regime of strong adhesion. The adhesion should, however, be much beyond $W = 10^{-6}$ for large flat membranes to pack into a volume equivalent to that of a typical cell. It has been pointed out [8], that the unbinding temperatures of biological membranes can appear at very reasonable temperatures so that binding and unbinding of membranes may play a role in biological systems. In such a case $T^* \ll \kappa$ so that folding, scrolling up or collapse as a result of thermal fluctuations is very unlikely.

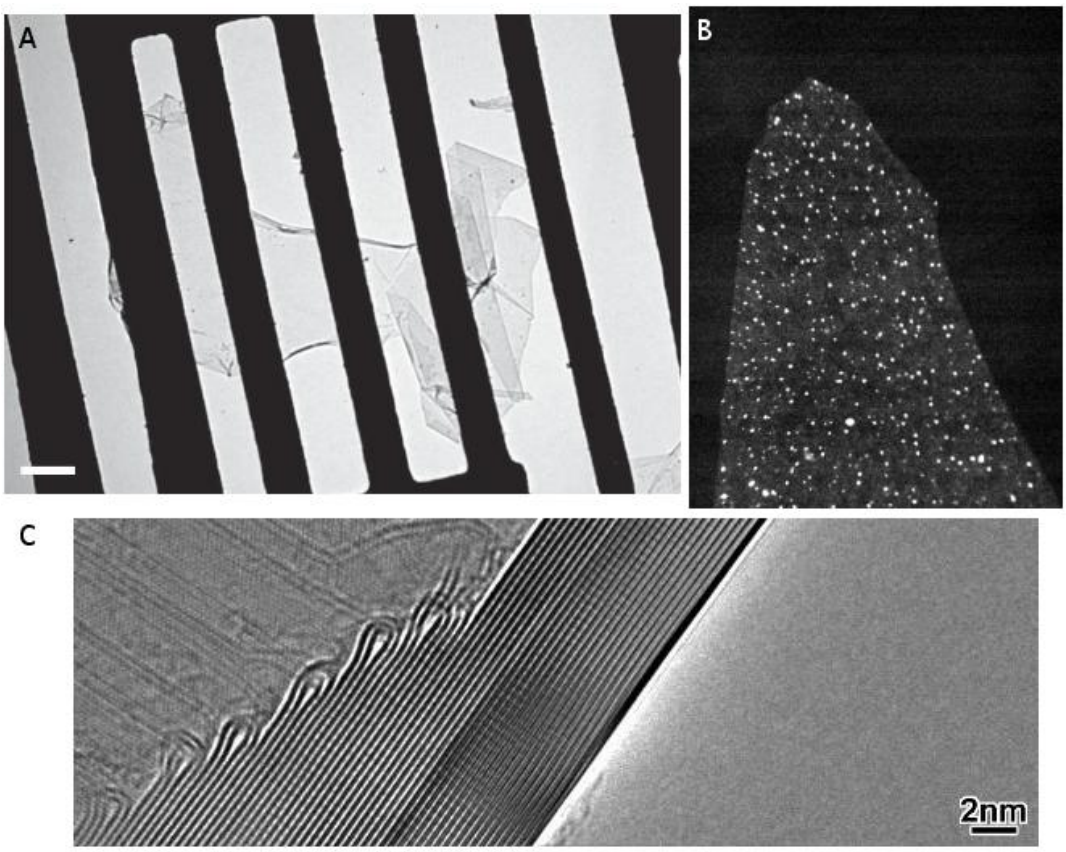

Figure 5.7: TEM images of graphene. (**A**) A freely suspended graphene flake. The top and bottom edges display scrolling and there is a folded region on the right. Scale bar, 500 nm. Reprinted by permission from Macmillan Publishers Ltd: J. Meyer *et al.*, Nature **446**, 60 (2007), copyright 2007. (**B**) A graphene flake supported only from the bottom edge. The size of the flake is approximately 3 by 5 μm. The bright dots are copper particles. Reprinted with permission from T. J. Booth *et al.*, Nano Lett. **8**, 2442 (2008). Copyright 2008 American Chemical Society. (**C**) Stacking graphene layers. Closed edges display folds of length $l \approx 4$ nm. Reprinted with permission from Z. Liu, K. Suenaga, P. J. Harris and S. Iijima, Phys. Rev. Lett. **102**, 015501 (2009), link.aps.org/doi/10.1103/PhysRevLett.102.015501. Copyright 2009 by the American Physical Society.

Graphene is another kind of membrane with fascinating properties (figure 5.7). It has a very high inplane stiffness [77], but in comparison its intrinsic bending rigidity is small. The bending modulus of a single layer graphene has been approximated as $\kappa \approx 1$ eV at room temperature [74]. The exfoliation energy 52 meV/atom [69] of graphene layers results in $W \approx 0.3$ J/m^2. These values of κ and W yield $L^* \approx 8$ nm, and a loop length l of only ≈ 4 nm. Loops of this size have been recently observed in graphene by transmission electron microscopy, see figure 5.7C. The adhesive membrane in figure 5.3 has $WL^2/\kappa = 10^4$ which for graphene would imply $L \approx 100$ nm. Graphene membranes can have L much larger than this, and thus the relative effect of adhesion would be even stronger. Graphene can sustain large strains elastically (up

to 10-20% [76]), which makes a fully elastic membrane model justified. The high stiffness and strong attraction of graphene suggest a very high unbinding temperature, at least several thousand Kelvin, giving no hope that folded, scrolled up or crumpled graphene could be released back to a flat state by heating. Although graphene has a strong attraction, its bending modulus is so high that some driving, other than just thermal fluctuations, might be required for the collapse of graphene. This is compatible with recent experiments, where free standing graphene has shown to be stable in a gas environment [76], see figure 5.7B, and sonification of graphene-liquid suspension was used to improve formation of scrolls [57]. There have been no reports on graphene membranes collapsing compactly to form small graphite particles, which seems reasonable as that would likely require strong external forcing.

6 Conclusions and outlook

In elastic materials crumpling was found independent of the width to thickness ratio of the sheet as far as solid volume fraction of the crumpled configuration is not too high. The energy of crumpled elastic sheets satisfies a scaling expression given by the scaling properties of a single ridge and the average ridge size. Similarity of elastic ridge patterns for varying thickness is expected to result from the ability of elastic structures to relax towards minimum energy configurations.

For elasto-plastic materials crumpling was found qualitatively different than in the elastic case. It is evident that for high enough width to thickness ratio an isolated elasto-plastic ridge behaves as an elastic one. However, high strain at the end vertices of the ridge exceeds the elastic limit of the sheet material. This means that a vertex in a crumpled elasto-plastic sheet cannot move without energetic cost. This hinders the elastic relaxation and a high number of ridges forms. As a result large elasto-plastic sheets are harder to crumple than their elastic counterparts. This is expected to be relevant for almost all real materials.

For membranes at microscopic scale we confirmed that thermal fluctuations do not induce crumpling. Thermally fluctuating membranes appear stiffer under externally forced crumpling, but this is overwhelmed by typically high deformation energies involved in crumpling. We demonstrated that membranes with van der Waals like adhesion can reach low energy configurations by scrolling or folding, but confining them into a small spherical volume requires as much effort than their non-adhesive counterparts. Temperature should be high and adhesion strong for such a membrane to collapse spontaneously without any guidance. We suggest that such a collapse is not realized in typical biological and atom-layer membranes, such as e.g. graphene.

There are several directions in which research on crumpling could be carried on. In simulations we were able to simulate sheets with a width to thickness ratio of $L/h \approx 1000$. Sheets that appear in nature are typically not of larger size, but artificial sheets, like graphene, can have much larger L/h. Predicting statistical properties of crumpling in the thermodynamic limit ($L/h \to \infty$) would benefit from large sheet sizes. They are computationally challenging because not only the number of lattice points grows with increasing L/h, but the effective stiffness of the sheet decreases such that compression of large sheets must be performed very slowly to avoid inertial effects. This problem could be partly resolved with an adaptive simulation lattice. Use of such a technique would be justified by the physics of crumpling, as a dense mesh is

only needed for a small fraction of the sheet, i.e. for sharp vertices and ridges. That fraction also decreases for incresing L/h. Another way to improve performance might be using an implicit method to solve the equations of motion instead of an explicit method [42]. This could allow significantly larger time steps, but implementation for crumpling applications would be far from trivial.

In elastic theory properties of isolated ridges and cones are already well established [37, 44, 47, 68], and buckling of single ridges have been analyzed [55]. However, in the simulations the main mechanisms of crumpling and in the formation of new ridges were buckling of relatively flat facets and splitting of vertices rather than buckling of ridges. This behaviour would deserve further analysis.

Finally, the geometry of full scale crumpling is an unexplored area. For example, we were able to approximate only by simulations how the average facet size behaves as a function of radius of the crumpled configuration. This size decreased faster than the radius. There are special ways that allow compactification of a sheet into a small volume without excessive stretching while retaining the facet size similar to that of the packed configuration [16, 12, 17]. Under simple confinement such packings may, however, be unattainable. For finite L/h the relaxation of curvature in ridges does not allow for the sharp folds obviously required for such 'geometrically clever' packings. In any case, the constraints set by self-avoidance and the fact that deformations in a thin sheet are nearly isometric, could somehow be utilized when constructing a geometrical theory of crumpling.

Appendix A: Box compression

Strength of cartons and thin-walled cylinders

Strength of a thin-walled box against compressive loading has practical importance in packaging. Boxes, typically made of paperboard or polymeric materials, are stacked reducing costs in transport and storage. An obvious requirement is that the lowest box must hold the load set by the boxes on top of it. A related problem is the axial loading of a thin-walled cylinder [1, 6]. Compression of a cylinder results in a uniform in-plane strain until a critical buckling load. At the critical load F_c the compressive strength reaches the maximum, and the cylinder collapses. For a material with Young's modulus Y, thickness h and Poisson's ratio $\nu = 0.3$, the critical load is [1, 6]

$$F_c = 3.8Yh^2. \tag{6.1}$$

The strength of a thin-walled cylinder is, however, sensitive to imperfections and the theoretical critical load (6.1) is practically difficult to achieve. A proposed empirical formula based on extensive data is [52]

$$F_c \approx 10\pi Yh^2 \left(\frac{h}{R}\right)^{0.5}, \tag{6.2}$$

where R is the radius of the cylinder. The formula was found valid for $100 \lesssim R/h \lesssim 3000$ [52].

The compressive strength of boxes made of paperboard, *i.e.* cartons, are often estimated by the Fellers formula [5, 9], by which the maximum strength of a carton is

$$F_b \approx 8\pi\sqrt{\sigma_{SCT}\sqrt{S_{MD}S_{CD}}}. \tag{6.3}$$

Here σ_{SCT} is the short compressive strength (SCT) measuring the ultimate in-plane strength, and $\sqrt{S_{MD}S_{CD}}$ is the geometric mean of the bending stiffnesses in the so called machine and cross directions of the paperboard. An equivalent formula for an isotropic material is found by writing $\sigma_{SCT} = \sigma_s Yh$ and $\sqrt{S_{MD}S_{CD}} = \kappa$. With $\nu = 0.3$ this results in

$$F_b \approx 8Yh^2\sqrt{\sigma_s}, \tag{6.4}$$

which is of the same form than F_c (6.1) for a cylinder, excluding the yield stress σ_s dependence. The derivation of equations (6.4) and (6.3) is based on the classical analysis

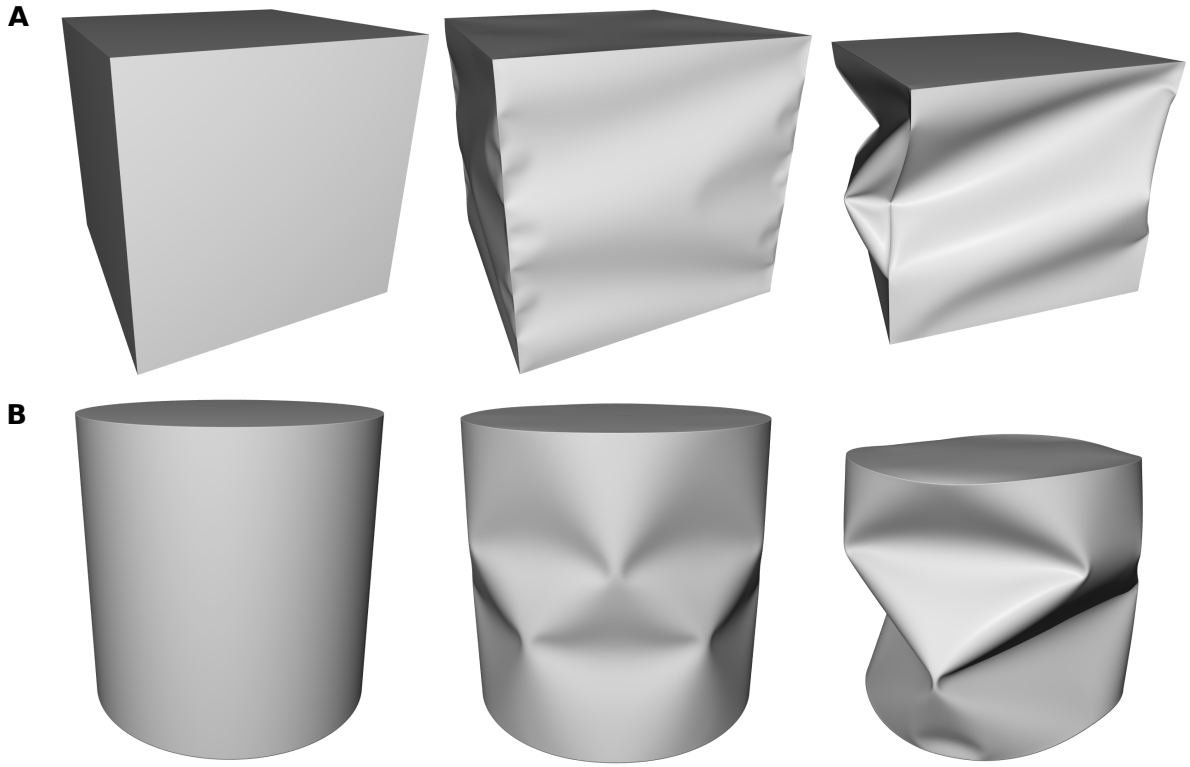

Figure 6.1: (**A**) Thin-walled box of size $L/h = 1000$ uncompressed (left), compressed by 1 % (middle) and by 10 % (right). (**B**) Thin-walled cylindrical can of size $R/h = 500$ uncompressed (left), compressed by 1 % (middle) and by 10 % (right).

of panel compression strength [1, 5]. For a box made of fully elastic material ($\sigma_s = \infty$) these results do not seem to be valid, and to this end we simulated the compression of an elastic box. We also compare briefly the box and cylinder compression.

Compressing an elastic box and cylindrical can

We modeled compression of an elastic thin-walled box ($L/h = 1000$) and cylindrical can ($R/h = 500$) by the model based on deformable elements (see Chapter 3). They had closed tops and bases, which were fastened along all their edges to the vertical faces. The compression was performed between two solid horizontal plates. The contact with the compressive plates was frictionless, and deformations of the tops and bases were not restricted in any way (simulations indicated that their deformation was rather meaningless for the compression strength).

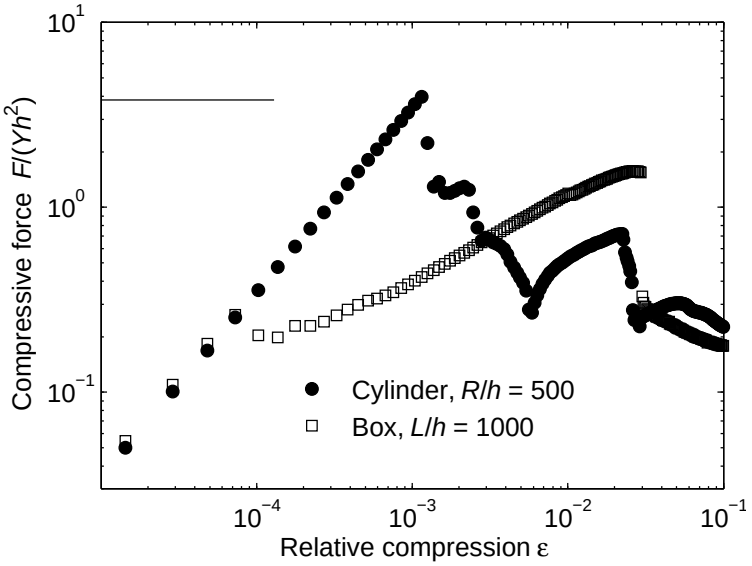

Figure 6.2: Compressive force F scaled by Yh^2 as a function of relative compression ϵ for a simulated box and cylinder. The theoretical critical load $F_c/(Yh^2) = 3.8$ for a cylinder is indicated by a line segment.

Simulated compression of the can was much as expected. There was a uniform in-plane compression in the beginning of the compression, after which the can abruptly collapsed. The resulting buckling pattern displayed familiar diamond shaped defects, see figure 6.1B. The maximal compression force agreed, within the accuracy of the simulation model, with the theoretical critical load for a cylinder, see figure 6.2. This was expected as the can had no imperfections.

The maximal compression force for the box was $F_b/(Yh^2) \approx 1.7$, *i.e.* about a half of that of the can. It was reached at a more than an order of magnitude higher compression (figure 6.2), which reflects a qualitative difference in compression of cylinders and boxes. Boxes under compression display out-of-plane buckling under compressive forces much less than their ultimate strength. The box compressed by 1 % in figure 6.1A is not yet collapsed, unlike the can below it at the same compression.

Simulations indicate that equations (6.3) and (6.4) are not valid for high yield stresses. This means that the relative importance of plastic yielding and elastic buckling for the box compression strength needs to be analyzed.

References

[1] S. P. Timoshenko and J. M. Gere, *Theory of Elastic Stability* (McGraw-Hill, Tokyo, 1961).

[2] M. J. Forray, *Variational Calculus in Science and Engineering* (McGraw-Hill, USA, 1968).

[3] L. D. Landau, *Theory of Elasticity, 2nd ed.* (Pergamon, Oxford, 1970).

[4] P. F. Byrd, M. D. Friedman, *Handbook of Elliptic Integrals for Engineers and Scientists* (Springer - Verlag, Berlin Heidelberg New York, 1971).

[5] C. Fellers *et al.*, *Carton board - the profitable use of pulps and processes* (STFI, Sweden, 1983).

[6] A. Pogorelov, *Bendings of surfaces and stability of shells* (American Mathematical Society, Providence, 1988).

[7] M. K. Hakala, *Lujuusopin elementtimenetelmä* (Otatieto, Espoo, 1994).

[8] R. Lipowsky and E. Sackmann, *Structure and dynamics of membranes* (Elsevier, Amsterdam, 1995).

[9] D. Hine, *Cartons and cartoning* (Pira, UK, 1999).

[10] T. Schlick, *Molecular Modeling and Simulation: An Interdisciplinary Guide* (Springer - Verlag, New York, 2002).

[11] D. C. Rapaport, *The Art of Molecular Dynamics Simulation* (Cambridge, 2004).

[12] D. R. Nelson, T. Piran and S. Weinberg, *Statistical Mechanics of Membranes and Surfaces, 2nd ed.* (World Scientific, Singapore, 2004).

[13] A. Munjiza, *The Combined Finite-Discrete Element Method* (Wiley, Chichester, 2004).

[14] C. Ericson, *Real-Time Collision Detection* (Morgan Kaufmann, San Francisco, 2004).

[15] K. Erleben, J. Sporring, K. Henriksen and H. Dohlmann, *Physics-Based Animation* (Charles River Media, 2005).

[16] E. D. Demaine and J. O'Rourke, *Geometric Folding Algorithms: Linkages, Origami, Polyhedra* (Cambridge, 2007).

[17] K. Miura, *Proceedings of the 31st Congress of the International Astronautical Federation, IAF-80-A 31*, (AIAA, New York, 1980).

[18] R. Lipowsky and S. Leibler, *Unbinding transitions of interacting membranes*, Phys. Rev. Lett. **56**, 2541 (1986).

[19] Y. Kantor, M. Kardar and D. R. Nelson, *Statistical mechanics of tethered surfaces*, Phys. Rev. Lett. **57**, 791 (1986).

[20] M. Kallay, *Plane curves of minimal energy*, ACM Transactions on mathematical software **12**(3), 219 (1986).

[21] Y. Kantor, M. Kardar and D. R. Nelson, *Tethered surfaces: Statics and dynamics*, Phys. Rev. A **35**, 3056 (1987).

[22] Y. Kantor and D. R. Nelson, *Phase transitions in flexible polymeric surfaces*, Phys. Rev. A **36**, 4020 (1987).

[23] M. A. F. Gomes, *Blackish fractal balls*, J. Phys. A **20**, 283 (1987).

[24] H. S. Seung and D. R. Nelson, *Defects in flexible membranes with crystalline order*, Phys. Rev. A **38**, 1005 (1988).

[25] M. Plischke and D. Boal, *Absence of a crumpling transition in strongly self-avoiding tethered membranes*, Phys. Rev. A **38**, 4943 (1988).

[26] R. Lipowsky, *Lines of renormalization group fixed points for fluid and crystalline membranes*, Europhys. Lett. **7**, 255 (1988).

[27] F. F. Abraham and D. R. Nelson, *Fluctuations in the flat and collapsed phases of polymerized membranes*, J. Phys. France **51**, 2653 (1990).

[28] F. F. Abraham and M. Kardar, *Folding and unbinding transitions in tethered membranes*, Science **252**, 419 (1991).

[29] R. Lipowsky, *The conformation of membranes*, Nature **349**, 475 (1991).

[30] D. Liu and M. Plischke, *Monte Carlo studies of tethered membranes with attractive interactions*, Phys. Rev. A **45**, 7139 (1992).

[31] D. M. Kroll and G. Gompper, *The conformation of fluid membranes: Monte Carlo simulations*, Science **255**, 968 (1992).

[32] C. F. Schmidt *el al.*, *Existence of a flat phase in red cell membrane skeletons*, Science **259**, 952 (1993).

[33] T. A. Witten and H. Li, *Asymptotic shape of a fullerene ball*, Europhys. Lett. **23**, 51 (1993).

[34] M. S. Spector, E. Naranjo, S. Chiruvolu and J. A. Zasadzinski, *Conformations of a tethered membrane: Crumpling in graphitic oxide?*, Phys. Rev. Lett. **73**, 2867 (1994).

[35] F. Meyer, *Topographic distance and watershed lines*, Signal processing **38**, 113 (1994).

[36] G. S. Grest and I. B. Petsche, *Molecular dynamics simulations of self-avoiding tethered membranes with attractive interactions: Search for a crumpled phase*, Phys. Rev. E **50**, 1737 (1994).

[37] A. E. Lobkovsky, S. Gentges, H. Li, D. Morse and T. A. Witten, *Scaling properties of stretching ridges in a crumpled elastic sheet*, Science **270**, 1482 (1995).

[38] P. A. Houle and J. P. Sethna, *Acoustic emission from crumpling paper*, Phys. Rev. E **54**, 278 (1996).

[39] E. M. Kramer and A. E. Lobkovsky, *Universal power law in the noise from a crumpled elastic sheet*, Phys. Rev. E **53**, 1465 (1996).

[40] A. E. Lobkovsky, *Boundary layer analysis of the ridge singularity in a thin plate*, Phys. Rev. E **53**, 3750 (1996).

[41] E. M. Kramer and T. A. Witten, *Stress condensation in crushed elastic manifolds*, Phys. Rev. Lett. **102**, 1303 (1997).

[42] D. Baraff and A. Witkin, *Large steps in cloth simulation*, Proc. of SIGGRAPH, 43 (1998).

[43] D. Moldovan and L. Golubovic, *Buckling dynamics of compressed thin sheets (membranes)*, Phys. Rev. Lett. **82**, 2884 (1999).

[44] E. Cerda, S. Chaieb, F. Melo and L. Mahadevan, *Conical dislocations in crumpling*, Nature **401**, 46 (1999).

[45] M. Desburn, M. Meyer, P. Schroeder and A. Barr, *Implicit fairing of irregular meshes using diffusion and curvature flow* Proc. of SIGGRAPH, 317 (1999).

[46] S. C. Venkataramani, T. A. Witten, E. M. Kramer and R. P. Geroch, *Limitations on the smooth confinement of an unstretchable manifold*, J. Math. Phys. **41**, 5107 (2000).

[47] A. Boudaoud, P. Patricio, Y. Couder and M. Ben Amar, *Dynamics of singularities in a constrained elastic plate*, Nature **407**, 718 (2000).

[48] M. J. Bowick, A. Cacciuto, G. Thorleifsson and A. Travesset, *Universality classes of self-avoiding fixed-connectivity membranes*, Eur. Phys. J. E **5**, 149 (2001).

[49] M. J. Bowick and A. Travesset, *The statistical mechanics of membranes*, Phys. Rep. **344**, 255(2001).

[50] B. A. DiDonna and T. A. Witten, *Anomalous strength of membranes with elastic ridges*, Phys. Rev. Lett. **87**, 206105 (2001).

[51] B. A. DiDonna, T. A. Witten, S. C. Venkataramani and E. M. Kramer, *Singularities, structures, and scaling in deformed m-dimensional elastic manifolds*, Phys. Rev. E **65**, 016603 (2002).

[52] E. Zhu, P. Mandal and C. R. Calladine, *Buckling of thin cylindrical shells: an attempt to resolve a paradox*, Int. J. Mech. Sci. **44**, 1583 (2002).

[53] K. Matan, R. B. Williams, T. A. Witten and S. R. Nagel, *Crumpling a thin sheet*, Phys. Rev. Lett. **88**, 076101 (2002).

[54] T. Mora and A. Boudaoud, *Thin elastic plates: On the core of developable cones*, Europhys. Lett. **59**, 41 (2002).

[55] B. A. DiDonna, *Scaling of the buckling transition of ridges in thin sheets*, Phys. Rev. E **66**, 016601 (2002).

[56] R. Bridson, R. Fedkiw and J. Anderson, *Robust treatment of collisions, contact and friction for cloth animation*, Proc. of SIGGRAPH, 594 (2002).

[57] L. M. Viculis, J. J. Mack and R. B. Kaner, *A Chemical route to carbon nanoscrolls*, Science **299**, 1361 (2003).

[58] J. A. Åström, J. Timonen and M. Karttunen, *Crumpling of a stiff tethered membrane*, Phys. Rev. Lett. **93**, 244301 (2004).

[59] T. Liang and T. A. Witten, *Crescent singularities in crumpled sheets*, Phys. Rev. E **71**, 016612 (2005).

[60] D. L. Blair and A. Kudrolli, *Geometry of crumpled paper*, Phys. Rev. Lett. **94**, 166107 (2005).

[61] K. S. Novoselov *et al.*, *Two-dimensional atomic crystals*, PNAS **102**, 10451 (2005).

[62] S. Chaieb, V. K. Natrajan and A. A. El-rahman, *Glassy conformations in wrinkled membranes*, Phys. Rev. Lett. **96**, 078101 (2006).

[63] G. A. Vliegenthart and G. Gompper, *Forced crumpling of self-avoiding elastic sheets*, Nature Mat. **5**, 216 (2006).

[64] E. Sultan and A. Boudaoud, *Statistics of crumpled paper*, Phys. Rev. Lett. **96**, 136103 (2006).

[65] M. Alava and K. Niskanen, *The physics of paper*, Rep. Prog. Phys. **69**, 669 (2006).

[66] T. Gruhn, T. Franke, R. Dimova and R. Lipowsky, *Novel method for measuring the adhesion energy of vesicles*, Langmuir **23**, 5423 (2007).

[67] J. Meyer *et al.*, *The structure of suspended graphene sheets*, Nature **446**, 60 (2007).

[68] T. A. Witten, *Stress focusing in elastic sheets*, Rev. Mod. Phys. **79**, 643 (2007).

[69] S. Grimme, C. Mück-Lichtenfeld and J. Antony, *Noncovalent interactions between graphene sheets and in multishell (hyper)fullerenes*, J. Phys. Chem. C **111**, 11199 (2007).

[70] M. A. F. Gomes *el al.*, *Structural properties of crumpled cream layers*, J. Phys. D **40**, 3665 (2007).

[71] A. S. Balankin, I. C. Silva, O. A. Martinez and O. S. Huerta, *Scaling properties of randomly folded plastic sheets*, Phys. Rev. E **75**, 051117 (2007).

[72] C. A. Andresen, A. Hansen and J. Schmittbuhl, *Ridge network in crumpled paper*, Phys. Rev. E **76**, 026108 (2007).

[73] A. S. Balankin, R. C. M. de Oca and D. S. Ochoa, *Intrinsically anomalous self-similarity of randomly folded matter*, Phys. Rev. E **76**, 032101 (2007).

[74] A. Fasolino, J. H. Los and M. I. Katsnelson, *Intrinsic ripples in graphene*, Nature Mat. **6**, 858 (2007).

[75] N. Stoop, F. K. Wittel and H. J. Herrmann, *Morphological phases of crumpled wire*, Phys. Rev. Lett. **101**, 094101 (2008).

[76] T. J. Booth *et al.*, *Macroscopic graphene membranes and their extraordinary stiffness*, Nano Lett. **8**, 2442 (2008).

[77] C. Lee, X. Wei, J. W. Kysar and J. Hone, *Measurement of the elastic properties and intrinsic strength of monolayer graphene*, Science **18**, 385 (2008).

[78] Y. C. Lin, Y. L. Wang, Y. Liu and T. M. Hong, *Crumpling under an ambient pressure*, Phys. Rev. Lett. **101**, 125504 (2008).

[79] Z. Liu, K. Suenaga, P. J. Harris and S. Iijima, *Open and closed edges of graphene layers*, Phys. Rev. Lett. **102**, 015501 (2009).

[80] W. Cheng *et al.*, *Free-standing nanoparticle superlattice sheets controlled by DNA*, Nature Mat. **8**, 519 (2009).